A&A 641, A74 (2020)
https://doi.org/10.1051/0004-6361/202037795

Astronomy & Astrophysics

Pulsating chromosphere of classical Cepheids

Calcium infrared triplet and Hα profile variations⋆

V. Hocdé[1], N. Nardetto[1], S. Borgniet[2], E. Lagadec[1], P. Kervella[2], A. Mérand[3], N. Evans[4], D. Gillet[5], Ph. Mathias[6], A. Chiavassa[1], A. Gallenne[1], L. Breuval[2], and B. Javanmardi[2]

[1] Université Côte d'Azur, Observatoire de la Côte d'Azur, CNRS, Laboratoire Lagrange, France
e-mail: vincent.hocde@oca.eu
[2] LESIA, Observatoire de Paris, Université PSL, CNRS, Sorbonne Université, Université de Paris, 5 place Jules Janssen, 92195 Meudon, France
[3] European Southern Observatory, Karl-Schwarzschild-Str. 2, 85748 Garching, Germany
[4] Smithsonian Astrophysical Observatory, MS 4, 60 Garden St. Cambridge, MA 02138, USA
[5] Observatoire de Haute-Provence – CNRS/PYTHEAS/Université d'Aix-Marseille, 04870 Saint-Michel l'Observatoire, France
[6] IRAP, Université de Toulouse, CNRS, CNES, UPS, 14 Av. E. Belin, 31400 Toulouse, France

Received 21 February 2020 / Accepted 2 July 2020

ABSTRACT

Context. It has recently been shown that the infrared (IR) emission of Cepheids, constant over the pulsation cycle, might be due to a pulsating shell of ionized gas with a radius of about 15% of that of the star radius, which could be attributed to the chromospheric activity of Cepheids.
Aims. The aim of this paper is to investigate the dynamical structure of the chromosphere of Cepheids along the pulsation cycle and to quantify its size.
Methods. We present Hα and calcium near-infrared triplet (Ca IR) profile variations using high-resolution spectroscopy with the UVES spectrograph of a sample of 24 Cepheids with a good period coverage from ≈3 to 60 days. After a qualitative analysis of the spectral line profiles, we quantified the Van Hoof effect (velocity gradient between the Hα and Ca IR) as a function of the period of the Cepheids. We then used the Schwarzschild mechanism (a line doubling due to a shock wave) to quantify the size of the chromosphere.
Results. We find a significant Van Hoof effect for Cepheids with a period larger than $P = 10$ days. In particular, Hα lines are delayed with a velocity gradient up to $\Delta v \approx 30$ km s^{-1} compared to Ca IR. By studying the shocks, we find that the size of the chromosphere of long-period Cepheids is of at least ≈50% of the stellar radius, which is consistent at first order with the size of the shell made of ionized gas previously found from the analysis of IR excess. Last, for most of the long-period Cepheids in the sample, we report a motionless absorption feature in the Hα line that we attribute to a circumstellar envelope that surrounds the chromosphere.
Conclusions. Analyzing the Ca IR lines of Cepheids is of importance to potentially unbias the period–luminosity relation from their IR excess, particularly in the context of forthcoming observations of radial velocity measurements from the Radial Velocity Spectrometer on board *Gaia*, which could be sensitive to their chromosphere.

Key words. shock waves – techniques: spectroscopic – stars: variables: Cepheids – stars: chromospheres

1. Introduction

Cepheids are milestones of the extragalactic distance scale since their period and luminosity are correlated, which is known as the Leavitt law (Leavitt 1908) and is also referred to as the period–luminosity (PL) relation. These variable stars have provided among the most essential advances in the history of astronomy from the discovery of galaxies to the expansion of the Universe (Hubble 1926, 1929). Still today, the discovery of the accelerated expansion of the Universe (Riess et al. 1998) has demonstrated the central importance of Cepheids in modern astronomy. However, uncertainties on both zero point and slope of the PL relation are today one of the largest contributors to the error on the extragalactic distance ladder and therefore on the determination of H0, the Hubble-Lemaître constant (Riess et al. 2019).

A plausible source of uncertainty could be due to the infrared (IR) excess emitted by a circumstellar envelope (CSE) such as the ones discovered using long-baseline interferometry (Kervella et al. 2006; Mérand et al. 2006) in the K-band. However the origin and the nature of these CSEs are still debated. In particular, while CSE emission is explained by dust emission in some cases (Gallenne et al. 2012, 2013; Groenewegen 2020), it fails to reproduce the IR excess in other studies (Schmidt 2015).

The extended and dynamical atmosphere of Cepheids could be at the origin for the observed IR excess. Recently, Hocdé et al. (2020) analytically modeled free-free and bound-free emission from a thin shell of ionized gas to explain the near and mid-IR (MIR) excess of Cepheids. This shell is modeled with a size of about 15% of the star radius, whatever the pulsation phase, which corresponds to the region of the lower chromosphere.

In this model, the ionized material could be provided by periodic shocks occurring in the atmosphere, which heat up and ionize the gas.

⋆ Based on observations made with ESO telescopes at Paranal observatory under program IDs: 098.D-0379(A), 0100.D-0397(A) and 0101.D-0551(A).

Shocks in the radially pulsating atmosphere of Cepheids have been largely studied in the Hα Balmer line, providing valuable insight into the atmosphere dynamics (Breitfellner & Gillet 1993a,b,c; Nardetto et al. 2008; Gillet 2014). These studies have also been supported by radiative hydrodynamic models (Fokin 1991; Fokin et al. 1996; Fadeyev & Gillet 2004) which have demonstrated how the shock waves are generated then propagated through the atmosphere during a pulsation cycle. These studies emphasize the fundamental differences between the dynamics of short-, medium-, and long-pulsation-period Cepheids. In addition, the Hα emissions reported in the latter studies, in particular in the upper atmosphere of long-period Cepheids, could indicate a chromospheric emission of pulsational origin.

The chromospheric activity of Cepheids was first probed using the optical Ca II K line (Wilson & Vainu Bappu 1957; Kraft 1957) which showed transitory emissions after minimum light, with an increasing duration and strength with pulsation period. Later, upper chromospheric emission was detected on β Dor using ultraviolet Mg II h and k (Schmidt & Weiler 1979) followed by Schmidt & Parsons (1982, 1984) who found heterogeneous emission in the chromosphere with both rising and falling materials traveling through a tenth of the star's radius.

Later, in the outermost part of the chromosphere, Sasselov & Lester (1994a) observed a steady outflow of infrared HeI λ10830 absorption line, while time-dependent and nonlocal thermodynamic equilibrium (NLTE) hydrodynamic modeling constrained using previously published observational data (Sasselov & Lester 1994b,c) shows that the upper chromosphere should be permanently heated by an acoustic or magneto-hydrodynamic energy provided by means of convection. Hence, a combination of both low-frequency excitation provided by pulsational shocks and persistent high-frequency acoustic heating from turbulent convection cells seem to be responsible for the chromospheric dynamics. Others mechanisms leading to high-temperature plasmas (10^6 K) are not excluded. Indeed Bohm-Vitense & Parsons (1983) possibly detected X-ray emission in the spectra of ζ Gem, probably due to chromospheric activity, which was later confirmed around $\phi = 0.5$ in the case of δ Cep and β Dor (Engle et al. 2017). Although several heating mechanisms to produce such an amount of energy are considered, for example fast-moving shocks or magnetic reconnections, a coherent physical explanation remains to be found.

Alternative lines for probing upper atmosphere dynamic and chromospheric activity are provided by the calcium infrared triplet (λ8498.018, 8542.089 and 8662.140 Å). Indeed, Linsky et al. (1970) were the first to show that Ca IR lines from the Sun are formed in the lower chromosphere. These lines are also sensitive to the temperature because they are collisionally controlled like Ca H and K lines, between which an empirical correlation has been determined (Martin et al. 2017). These properties make Ca IR a suitable indicator of chromospheric activity (Linsky et al. 1979; Foing et al. 1989; Chmielewski 2000; Busà et al. 2007). While the emission in the core is generally weaker than other chromospheric indicators, these lines confer an advantage in that they are not blended by circumstellar or interstellar absorption, contrary to Ca H and K, and Mg II h and k. A series of papers on the solar chromosphere also highlights the importance of studying Ca IR complementary to Hα for probing the chromospheric activity (Cauzzi et al. 2008, 2009; Vecchio et al. 2009; Reardon et al. 2009). Indeed, as shown by Vernazza et al. (1973), the formation region of Hα and Ca IR covers most of the low chromosphere in the Sun. Therefore, it is interesting to use modern high-resolution instrument capabilities to observe Ca IR complementary to the Hα line for studying the pulsating chromosphere of classical Cepheids.

In addition, Ca IR lines were recently used to measure radial velocities (RVs) in Cepheids' atmospheres (Wallerstein et al. 2015, 2019). Indeed, as stated by Wallerstein et al. (2019), since the Radial Velocity Spectrometer (RVS) of ESA *Gaia* survey observes in the same wavelength range (Munari 1999; Sartoretti et al. 2018; Katz et al. 2019), it is of prime importance to understand the dynamic of these lines for Cepheid RV measurement accuracy, in particular in the context of the use of the Baade-Wesselink method for extragalactic distance scale measurement. The present paper is structured as follows. We first present the UVES[1] high-resolution profiles of Hα and Ca IR for the 24 Cepheids in our sample in Sect. 2. We analyze Hα and Ca IR profile variations in Sects. 3 and 4, respectively. In Sect. 5, we study the dynamics of the chromosphere from the Van Hoof effect. We finally estimate the size of the chromosphere from the Schwarzschild mechanism observed in Ca IR in Sect. 6. We then discuss our results in Sect. 7 and conclude in Sect. 8.

2. UVES observations and data reduction

2.1. Observations and data reduction

We gathered 1350 high-resolution ($R \sim 75\,000$) spectra from 24 Cepheids acquired with the red arm (~570 to ~940 nm wavelength range) of the UVES spectrograph (Dekker et al. 2000) mounted on the UT2 telescope at the Very Large Telescope (VLT). The processing and normalization of these spectra are detailed in Borgniet et al. (2019). We acquired several consecutive spectra (up to a dozen) at each observing epoch. The total number of distinct observing epochs is 193 over the whole data sample, with an average number of 8 epochs per target. The total number of epoch per target is indicated in Table 1. The average signal-to-noise ratio (S/N) per single spectrum is ≈100. In order to discuss the spectral line profiles qualitatively, at a given epoch we consider only the first snapshot of a series, without averaging the consecutive spectra. We consider the different observing epochs to be part of a unique pulsation cycle for each target, despite possible cycle-to-cycle variations (Anderson 2016). To study the line profile variations, we focus on the core of each line, hence we consider the same RV window ranging from −200 to 200 km s^{-1} and centered on the line rest wavelength corrected by the star center-of-mass velocity (also called γ-velocity, V_γ). The V_γ values we consider in the following analysis are listed in Table 1. We present a UVES spectrum centered on the Ca IR triplet in Fig. 1. AX Cir (5.27d), S Nor (9.75d), and VZ Pup (23.17d) are considered as prototypes of small-, mid-, and long-periods, respectively, in the remainder of the paper because of their good phase coverage (see Figs. 2–4) and recent ephemeris (see Table 1) presented in the following section.

2.2. Ephemeris

It is essential to use accurate ephemerides to analyze the profile variations of Cepheids along their pulsation cycle with precision. The ephemerides of Cepheids are characterized by their pulsation period P and their referenced epoch T_0 given at maximum light. However, since Cepheids undergo period change with time depending on evolutionary state (Turner et al. 2006), it is necessary to use ephemerides with a reference epoch which

[1] Ultra Violet and Echelle Spectrograph project developed by the European Southern Observatory.

Table 1. γ-velocities of the stars in the sample are indicated together with the corresponding references.

Star	γ (km s^{-1})	Ref.	P (days)	T_0 (MJD)	Ephemeris	UVES epoch
AV Cir	8.7 ± 1.6	(1)	3.065255	56 890.9571	G18	10
BG Cru	-19.3 ± 2.2	(2)	3.342477	56 965.8567	G18	6
RT Aur	20.3 ± 0.3	(2)	3.728313	47 956.8877	SPIPS	7
AH Vel	26.0 ± 2.9	(2)	4.226461	56 915.1433	G18	7
AX Cir	-20.9 ± 4.6	(2)	5.275967	56 887.7452	G18	8
MY Pup	11.0 ± 2.9	(2)	5.692962	56 948.3850	G18	7
EW Sct	-18.6 ± 0.3	(2)	5.82363	49 705.23	AAVSO	9
U Sgr	2.8 ± 0.3	(2)	6.745332	48 336.5001	SPIPS	10
V636 Sco	9.1 ± 0.17	(3)	6.79671	40 364.392	GCVS	7
R Mus	3.8 ± 2.9	(2)	7.510276	56 912.6852	G18	6
S Mus	-1.9 ± 0.4	(3)	9.658900	56 867.6654	G18	7
β Dor	7.2 ± 0.7	(2)	9.842661	50 274.9261	SPIPS	5
S Nor	5.6 ± 0.05	(4)	9.753759	56 874.8021	SPIPS	7
ζ Gem	2.8 ± 0.2	(2)	10.149857	48 708.0588	SPIPS	6
TT Aql	3.0 ± 0.3	(2)	13.754750	48 308.5570	SPIPS	10
RU Sct	-4.8 ± 0.3	(2)	19.70445	48 335.5908	SPIPS	7
RZ Vel	24.1 ± 2.4	(2)	20.497635	56 875.8093	G18	5
WZ Car	-14.7 ± 2.7	(2)	23.01759	53 418.78	GCVS	10
VZ Pup	63.3 ± 2.7	(2)	23.172844	56 904.7167	G18	8
T Mon	30.4 ± 0.2	(2)	27.029570	43 783.7905	SPIPS	6
ℓ Car	3.3 ± 0.7	(2)	35.55783	50 583.7427	SPIPS	6
U Car	1.7 ± 2.3	(2)	38.717914	56 849.1763	G18	8
RS Pup	24.6 ± 0.5	(2)	41.464114	56 872.3158	G18	5
V1496 Aql	71.8 ± 5.8	(1)	65.3679	51 736.0660	(5)	8

Notes. The ephemeris (T_0, P) are retrieved either from Gaia Collaboration (2018, G18) SPIPS software, or the GCVS catalog. Otherwise, the ephemeris of EW Sct and V1496 Aql are retrieved from AAVSO and Berdnikov et al. (2004), respectively. The number of UVES epoch of observations is indicated in the last column. The Cepheids that we consider as prototypes in the following of the paper are indicated in bold.
References. (1) Gaia Collaboration (2018), (2) Gontcharov (2006), (3) Pourbaix et al. (2004), (4) Mermilliod et al. (2008), (5) Berdnikov et al. (2004).

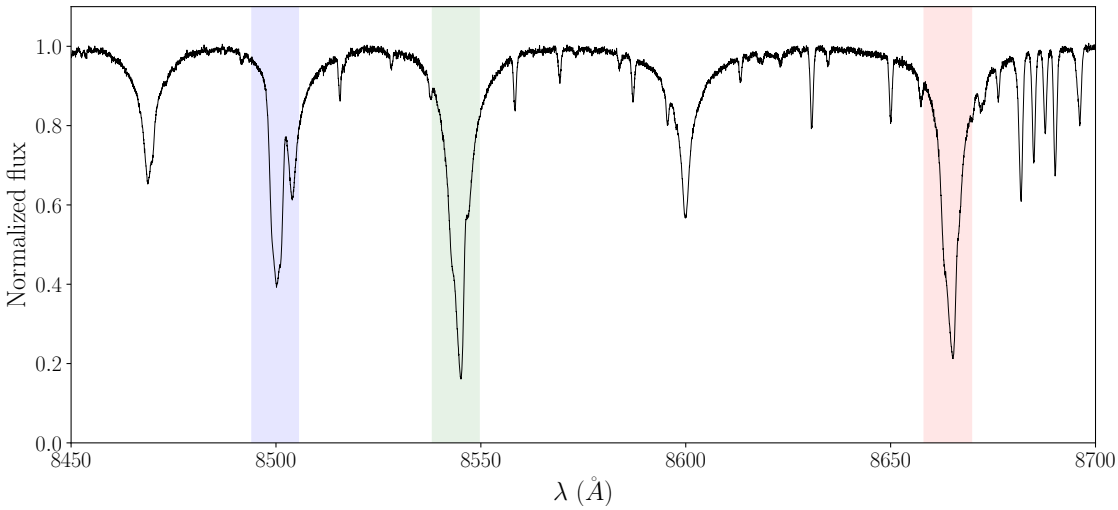

Fig. 1. Typical normalized UVES spectrum plotted over the RVS spectral window. The calcium IR triplet at 8498, 8552, and 8662 angstroms for VZ Pup at $\phi = 0.91$ is presented. In the following, the spectral line profiles are plotted over the [−200,+200] km s^{-1} velocity range, represented by vertical strips around each line.

is close to the UVES date of observation. The modified Julian date (MJD) of the UVES observations is approximately 58 000, which renders ephemerides obtained from Gaia Collaboration (2018) suitable. When these ephemerides are unavailable we use SpectroPhoto-Interferometric modeling of Pulsating Stars (SPIPS) which is a model-based parallax-of-pulsation code. SPIPS gathers multiple different data sets available in the literature from photometric, interferometric, effective temperature, and RV measurements in a robust model fit (Mérand et al. 2015). SPIPS was already extensively introduced and used in several studies (Mérand et al. 2015; Breitfelder et al. 2016; Kervella et al. 2017; Gallenne et al. 2017; Hocdé et al. 2020). When stars are not found in the precedent methods, which is the case for four stars, we retrieve data from the General Catalogue

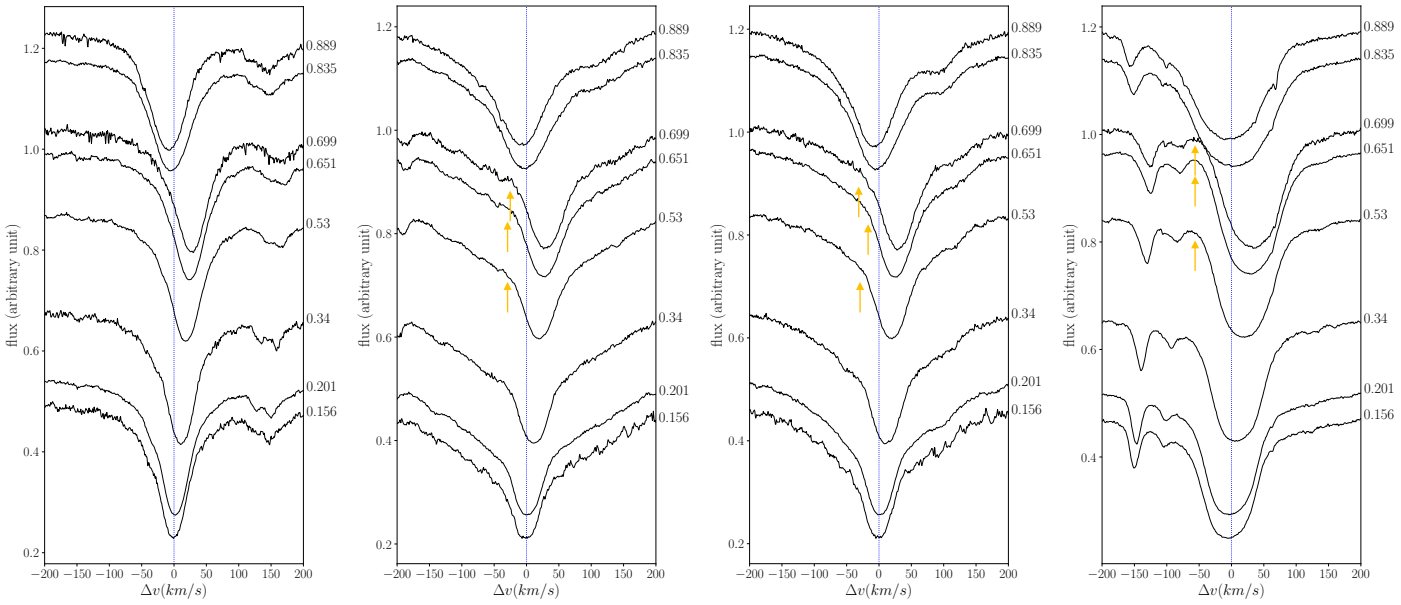

(a) λ8498 (b) λ8542 (c) λ8662 (d) Hα

Fig. 2. AX Cir, 5.27d. Colored arrows refer to remarkable features in these profiles and are also associated to the color from Fig. 6. The orange arrow highlights the blueshifted emission due to a blended inverse P Cygni profile.

of Variable Stars[2] (GCVS, Samus' et al. 2017) or the American Association of Variable Star Observers[3] (AAVSO, Watson et al. 2006). We note that older ephemeris could introduce a phase shift in the RV curves, in particular in the case of the long-period V1496 Aql which is known to present a significant stochastic period change (Berdnikov et al. 2004). The ephemeris are presented in Table 1 while profile variations are shown in Appendix B.

In the following sections, we proceed in two steps to analyze the data: we first describe the Hα profiles as an observational basis, and then we analyze Ca IR profiles.

3. Observational basis: Hα profile variations

In this section, we mostly confirm the Hα line behavior found in previous studies, but for a larger sample of 24 Cepheids with a good period coverage from $P \approx 3$ to 60 days.

3.1. Short-period Cepheids $P < 10$ d

Several studies have reported the quiescent behavior of Hα profiles of short-period cepheids which indeed present similar behavior to other metallic absorption lines (Schmidt 1970; Nardetto et al. 2008), while some authors have found differences at some phases (Jacobsen & Wallerstein 1981). The UVES observations of the ten short-period Cepheids in the sample confirm this general trend, with quiescent profiles during most of the pulsation cycle. At some phases, half of the short-period Cepheids present more disturbed features; in particular, a weak blueshifted emission is observed in the phase range $\phi = 0.6$–0.9 (see orange arrow in Fig. 2d). Because of the gravitational acceleration, upper atmosphere descending layers can reach supersonic velocities, producing an inward radiative shock. An inverse P Cygni profile could appear when the column density is important enough to contribute to the emission. However, the classical 0 km s^{-1} emission in the P Cygni profile is blended with deep photospheric absorption, resulting in an apparent blueshifted emission (see Fig. 5a). This emission in short-period Cepheids is followed by an important enlargement of the line profile, which is usually attributed to an increase of the turbulence during atmosphere compression (Breitfellner & Gillet 1993a; Fokin et al. 1996).

3.2. Medium-period Cepheids $P \approx 10$ d

Medium-period Cepheids differ from the short- and long-period Cepheids by the shape of their RV curve due to the Hertzsprung progression (Hertzsprung 1926). These Cepheids are indeed close to the $\omega_2/\omega_0 = 0.5$ resonance, where ω_0 and ω_2 are the periods corresponding to the fundamental and the second overtone modes, respectively (Kovacs et al. 1990). The UVES sample of medium-period Cepheids contains four stars, namely S Nor (our prototype), S Mus, ζ Gem, and β Dor, with a rather poor pulsation coverage. These stars have been studied by several authors (Bell & Rodgers 1967; Schmidt 1970; Jacobsen & Wallerstein 1982) who found substantial disturbed profiles and large displacement from metallic lines.

In the star sample, blueshifted Hα emission is observed in S Nor, S Mus, and β Dor around $\phi = 0.5$–0.6 (see orange arrow in Fig. 3d). As the atmosphere is infalling at these phases for resonance stars, an inverse P Cygni profile could appear if the gas is high enough and reaches supersonic velocities, as is the case for short- and long-period Cepheids.

In addition, S Nor and β Dor profiles are importantly wider around $\phi = 0.75$–0.80 (see Fig. 3d and Fig. B.11 respectively) with the appearance of a double absorption profile. These features are not observed on S Mus at phase $\phi = 0.9$ and there is no phase coverage beyond $\phi = 0.5$ for ζ Gem. The redshifted

[2] http://www.sai.msu.su/gcvs/gcvs/
[3] http://vizier.u-strasbg.fr/viz-bin/VizieR?-source=B/vsx

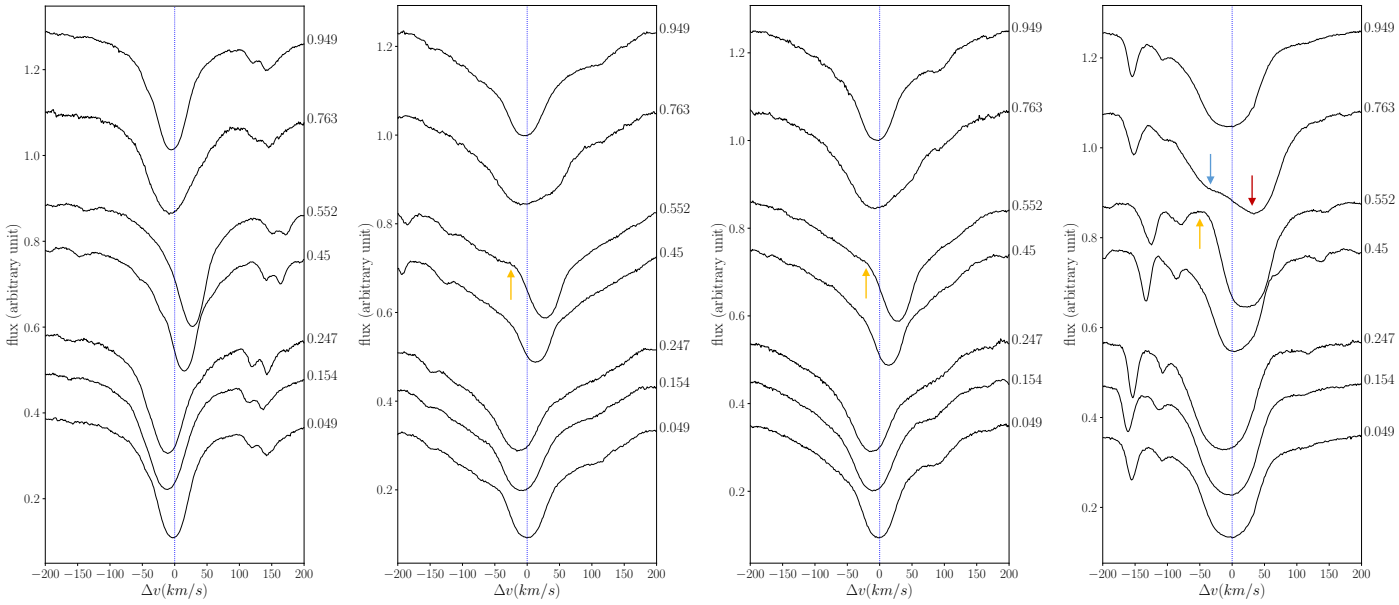

(a) λ8498 (b) λ8542 (c) λ8662 (d) Hα

Fig. 3. S Nor, 9.75d. The blue arrow is the blueshifted absorption due to the main shock. The red arrow is the redshifted absorption of the infalling atmosphere. Orange arrows are blueshifted emission due to a blended inverse P Cygni profile.

absorption in the profile (see red arrow in Fig. 3d) is caused by the infalling motion of the atmosphere while the blueshifted absorption is likely due to the main shock produced by the κ mechanism in the star interior, which later propagates outward into the atmosphere of the star. We therefore expect a collision between these infalling layers and the main shock, which could result in a line enlargement feature around $\phi = 0.8$.

3.3. Long-period Cepheids P > 10 d

For long-period Cepheids ($P > 10$ d), we confirm the global atmosphere dynamics from Hα profiles presented by Gillet (2014) in the case of X Cygni (16.3d). This latter author described three different Hα stages per cycle which are in agreement with the UVES observations of the ten long-period Cepheids presented in this paper:

1. From $\phi = 0.9$ to 0.3 when the photosphere is expanding, we observe the presence of a blueshifted Hα absorption (see blue arrows in Fig. 4d) which is identified as a gas flow at the rear of the main shock due to the κ-mechanism when emerging from the photosphere at $\phi \approx 0.85$ (see blue zone in Fig. 6a). This feature is accompanied by redshifted absorption due to the infalling atmosphere layers.

2. Between phase 0.9 and 0.5, a P Cygni profile is observed (see green arrows in Fig. 4d). This P Cygni profile is interpreted as Hα emission at the rear of the main shock front propagating outward; it appears as a P Cygni profile when it is sufficiently detached from the photosphere (see green zone in Fig. 6a). This feature progressively disappears between $\phi = 0.3$ and 0.6 and is no longer visible around $\phi \approx 0.6$ (see Figs. 4d and 6b).

3. From $\phi = 0.7$ to 0.9 a double absorption profile appears with blueshifted emission. This double absorption is composed of an absorption centered on the stellar rest frame and a redshifted absorption at $\approx$50 km s^{-1}. The motionless absorption feature has been attributed to a CSE by several authors, not only in the case of ℓ Car (Rodgers & Bell 1968; Baldry et al. 1997; Nardetto et al. 2008), but also in the case of the Type II long-period Cepheid W Virginis (Kovtyukh et al. 2011). On the other hand, the redshifted absorption is due to infalling layers of hydrogen during the ballistic motion. As a result, the blueshifted emission (orange arrows in Fig. 4d) is a blend between an inverse P Cygni profile caused by the supersonic infalling layers, and both a photospheric and a CSE absorption (see Fig. 5b).

4. From $\phi = 0.9$ to 1.0 the inverse P Cygni profile progressively disappears. Two effects could contribute together to explain this transition. First, since the layers are infalling, at a certain point they are not high enough in the atmosphere to produce a P Cygni profile. Secondly, the main shock emerges from the photosphere at phase $\phi \approx 0.85$, and then a blueshifted absorption may progressively blend the P Cygni emission.

4. Ca IR profile variations

In this section, we qualitatively describe and physically interpret Ca IR profile variations. We further show that Ca IR profile features are similar to Hα profile variations because they are induced by the same phenomena. We summarize our findings in Fig. 6 and Table 2.

4.1. Short-period cepheids P < 10 d

Similarly to Hα lines presented in Sect. 3.1, Ca IR profiles are almost quiescent during the pulsation cycle. However, a finer inspection reveals a weak blue-shifted emission between $\phi \approx 0.6$ and 0.9 which is always synchronized with Hα blue-shifted emission (see orange arrows in Fig. 2). Hence, we can infer that Ca IR blue-shifted emission has the same origin same origin as a Hα, the in-falling upper atmosphere layers are causing a radiative shock, resulting in an inverse P Cygni profile. The line λ8498 is less disturbed than the two others lines, a result that we find also for medium- and long-period Cepheids. According to Linsky et al. (1970) this line is formed lower in the chromosphere

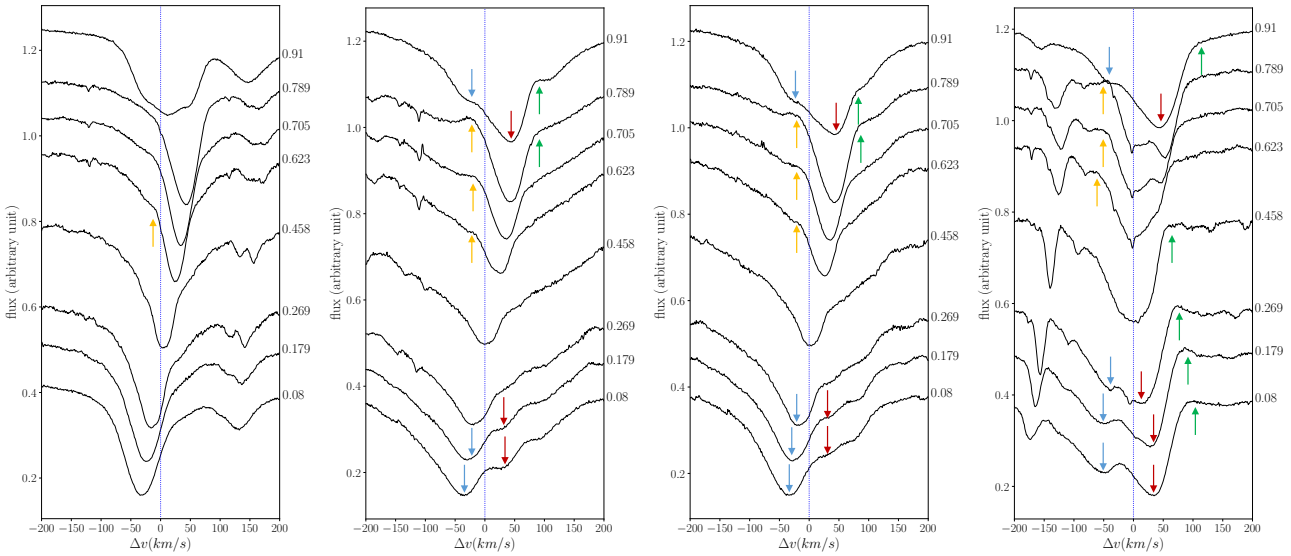

(a) λ8498 (b) λ8542 (c) λ8662 (d) Hα

Fig. 4. VZ Pup, 23.17d. Blue arrows show blueshifted absorption due to the main shock. Red arrows are redshifted absorption of the infalling atmosphere. Green arrows are redshifted emission due to a P Cygni profile. Orange arrows are blueshifted emission due to an inverse P Cygni profile.

than the two others. As a result, the acceleration is less important during ballistic movement of the atmosphere for line λ8498 and could be insufficiently high in the atmosphere to produce a P Cygni profile.

4.2. Medium-period Cepheids $P \approx 10$ d

In the case of medium-period Cepheids we also find the two profile features identified in the case of Hα profiles, that is a blueshifted emission followed by an enlargement of the lines (see Figs. 3b and c). However in this case it is less clear if we observe a simple enlargement due to turbulence or a double absorption profile which would be unresolved. Indeed, medium-period Cepheids are an intermediate case between short-period Cepheids dominated by the turbulence during the infalling motion and a double absorption profile as is the case in long-period Cepheids.

4.3. Long-period Cepheids $P > 10$ d

For all the profile variations presented in this paper we report the following Ca IR profile sequence over the pulsation period:

1. From $\phi = 0.9$ to 0.3 there are two important spectral features. First, we observe a double absorption profile centered on 0 km s^{-1} velocity. The same features were recently observed by Wallerstein et al. (2019) who published Ca IR profiles of X Cygni with a good phase coverage. We interpret this feature as a Schwarzschild mechanism (Schwarzschild 1952). Briefly, this phenomenon can be produced when two layers of an atmosphere with an opposite velocity field are colliding with each other. In the present case it is caused by the collision between the main shock expanding outward and the lower chromosphere region descending toward the photosphere (see Fig. 6a). Thus, both a blue- and a redshifted absorption component symmetrically centered on the stellar restframe are observed (see blue and red arrows respectively in Figs. 4b and c). This phenomenon is weaker or absent for the line λ8498. We study this behavior in detail in Sect. 6. Second, we also observe a redshifted emission (see green arrows in Figs. 4b and 4c). We attributed this feature to a P Cygni profile due to the radiative wake at the rear of the main shock (initiated at the end of the previous cycle) which is still propagating outward.

2. From $\phi = 0.3$ to 0.6 the main shock has reversed the atmosphere movement which is now expanding. The main shock continues to propagate, as shown in Fig. 6b, and all Ca IR profiles are passing through a quiescent phase. No particular features are observed.

3. Between $\phi = 0.6$ and 0.9 a blueshifted emission is observed (see orange arrows in Figs. 4a to c). In the case of VZ Pup, this emission is seen from $\phi = 0.623$ to 0.789 with increasing intensity, which is almost 20% of the pulsation cycle. Similarly to Hα, we attribute this feature to an inverse P Cygni profile due to the supersonic infalling movement of the atmosphere (see Fig. 6c). However, contrary to Hα it is not a double absorption profile. Indeed, since the abundance of calcium is lower than hydrogen, we expect weaker CSE absorption from Ca IR in long-period Cepheids. We propose that this observed emission could contribute enough in some cases to blend a part of the Ca IR emission as is the case in the sample for U Car and ℓ Car in Figs. B.18 and B.19.

As a conclusion from the analysis of the Ca IR profiles in the entire star sample, the presence of Ca IR emissions indicates chromospheric activity in the Cepheid upper atmosphere (Busà et al. 2007). Hence, the chromosphere is activated either by shocks during the infalling movement of the atmosphere or by the main shock propagating outward. In cases of long-period Cepheids, this emission is also observed for a significant part of the pulsation cycle ($\Delta\phi \approx 0.2$).

5. Chromosphere kinematics using Van Hoof effect

By studying solar chromosphere, Vernazza et al. (1973) derived a Hα core formation height higher than Ca IR. In addition, according to Linsky et al. (1970), the core of Ca λ8498 is formed

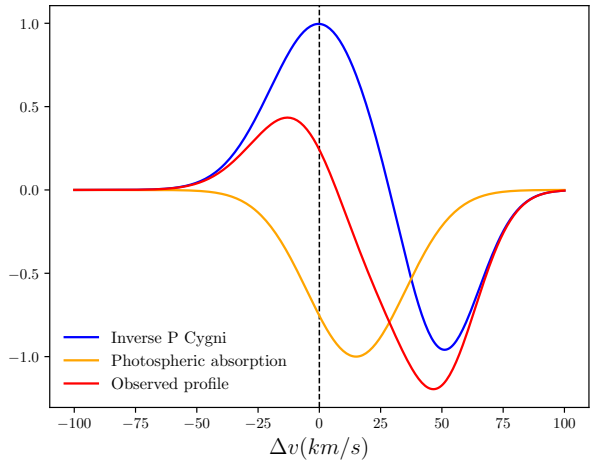

(a) Inverse P Cygni blended with photosphere

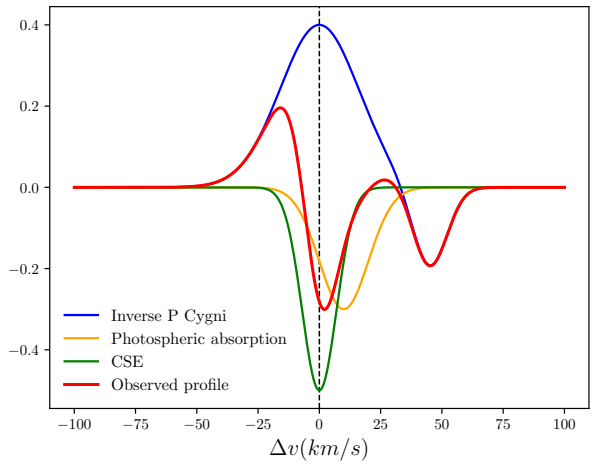

(b) Inverse P Cygni blended with CSE + photosphere

Fig. 5. Schematic profile formation of a blended inverse P Cygni profile. *Panel a*: the supersonic (≈50 km s^{-1}) descending atmospheric layers produce a radiative emission centered on 0 km s^{-1} (blue curve). This profile is blended with photospheric redshifted (≈15 km s^{-1}) absorption (orange curve) resulting in an apparently weak blueshifted emission. *Panel b*: in long-period Cepheids, a component centered on 0 km s^{-1} is attributed to a CSE (green) and causes the appearance of a double absorption profile.

lower than the other calcium lines in the chromosphere. Hence, by comparing Ca λ8498 and Hα core formation layers from Cepheids, we expect to directly obtain information on the velocity gradient between the bottom and the top of the chromosphere. In order to study the motion of the chromospheric layers we derive heliocentric RV curves of Ca λ8498 and Hα by measuring the minimum of the line. Therefore, we probe the RV associated to the core-forming region. When a double profile absorption is observed, as is the case in VZ Pup, we consider only the redshifted absorption, because it is produced by the atmospheric layers. We present the results in Fig. 7.

From these figures, Hα line and Ca λ8498 are well synchronized in the case of the short-period AX Cir, whereas the variation of Hα is late with respect to Ca λ8498 in S Nor and VZ Pup. This de-synchronization is similar to the Van Hoof effect (van Hoof & Struve 1953) in the case of hydrogen and metallic lines. This phenomenon is interpreted as an outward propagating wave all along the pulsation cycle (Mathias & Gillet 1993). We demonstrate the global de-synchronization of the chromospheric layers due to the propagation of waves for mid- and long-period Cepheids. Acceleration of Ca IR and Hα are almost identical in the case of AX Cir, which is likely a sign of a compact chromosphere due to the higher gravity field in short-period Cepheids. For both S Nor and VZ Pup, we observe an infalling movement which accelerates up to about 30 km s^{-1}. A sudden reverse from infalling (>0 km s^{-1}) to outward motion (<0 km s^{-1}) is then observed around 0.7 in case of S Nor while this appears later for VZ Pup at $\phi \approx 0.9$. For long-period Cepheids, we hypothesize that the reversal in motion of the atmosphere occurs later due to larger ballistic motion in Cepheids of lower gravity field. Furthermore, Ca IR lines first reverse their movement followed by Hα lines (see red and blue curves in Fig. 7). The larger de-synchronization for longer period Cepheids is likely responsible for the Schwarzschild mechanism in Ca IR that we study in Sect. 6.

In order to explore the link between the periods of Cepheids and upper atmosphere de-synchronization in the entire star sample, we derive the norm of the velocity gradient between Ca IR and Hα spectral lines, averaged over the pulsation cycle:

$$\Delta v = \frac{1}{N} \sum_{i=1}^{N} |V_{\lambda 8498}(\phi_i) - V_{\mathrm{H}\alpha}(\phi_i)|, \quad (1)$$

where $V_{\lambda 8498}$ and $V_{\mathrm{H}\alpha}$ are RVs of Ca IR and Hα measured using the minimum of the line profile, and N is the total number of pulsation phase. We also adopted the standard error of the mean s for N epoch in a pulsation cycle:

$$s = \frac{\sigma(\Delta v)}{\sqrt{N}}, \quad (2)$$

where $\sigma(\Delta v)$ is the standard deviation of the mean. The result is presented in Fig. 8.

Since the pulsation cycle coverage is relatively poor in the star sample, the Δv quantity (Eq. (1)) does not cover the full pulsation cycle and depends on the specific phases of observation. However, from Fig. 8 we can clearly observe a tendency towards two distinct regimes:

1. For Cepheids with period $P < 10$d, the layers associated to the top of line-forming regions of Ca IR and Hα, respectively, are synchronized (with $\Delta v < 5$ km s^{-1}.)

2. A sudden increase appears for $P \approx 10$d with a velocity gradient of the Hα layer compared to Ca IR rising up to 30 km s^{-1}.

6. Size of the chromosphere estimated from the Schwarzschild mechanism of long-period Cepheids

We observe the Schwarzschild phenomenon for eight out of ten long-period Cepheids (Schwarzschild 1952) between $\phi = 0.9$ and 0.3. Indeed, the observed profiles follow the classical picture of the Schwarzschild scenario in which the center-of-mass velocity falls in between the blue and red peaks. Moreover, since Linsky et al. (1970) found that the Ca λ8498 line is formed lower in the chromosphere than Ca λ8542 and λ8662 spectral lines, we can infer that Ca λ8498 is colliding first onto the main shock, which is confirmed by the fact that it is always in a more advanced stage in the Schwarzschild scenario than Ca λ8542 or λ8662 (see e.g. Fig. 4). Although we cannot firmly conclude

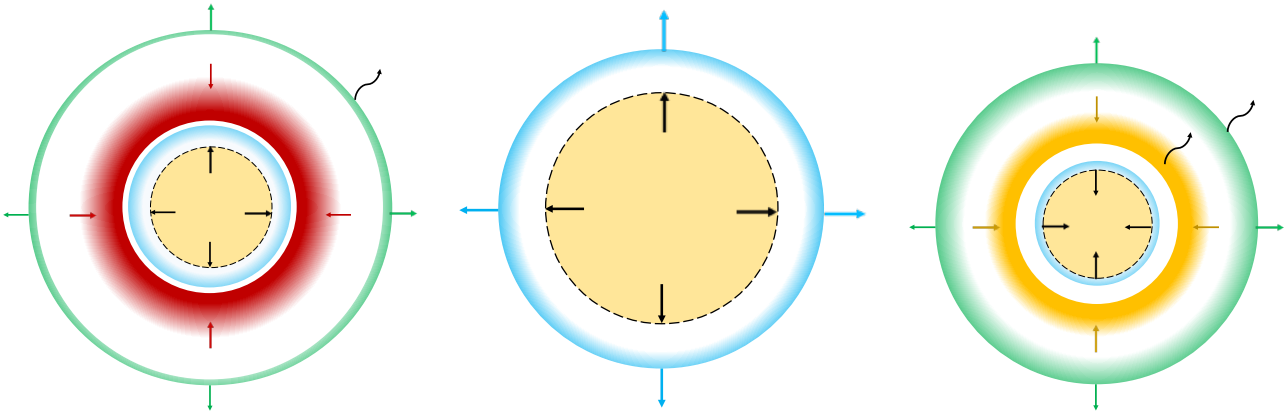

(a) ϕ=0.9-0.3 : Schwarzschild scenario (b) ϕ=0.3-0.6 : Quiescent profiles (c) ϕ=0.6-0.9 : Inverse P Cygni

Fig. 6. General scheme of the pulsating chromosphere dynamics from Ca IR variations. *Panel a*: as the main shock continues to propagate outward causing a radiative wake (black arrow emitted by the green zone), Hα exhibits a blended P Cygni profile. At the same time, a blueshifted absorption appears from the emerging main shock from the κ mechanism (blue zone). This shock collides with the Ca IR infalling layers (red zone), producing a Schwarzschild profile (Sect. 6). *Panel b*: quiescent phase: main shock has reversed the movement of the atmosphere which is now entirely propagating outward. The Hα P Cygni profile progressively disappears around $\phi = 0.5$. *Panel c*: following a ballistic motion, layers of the atmosphere fall onto the star (orange area). Supersonic velocities are reached if the acceleration is strong enough and thus an inverse P Cygni profile appears for Hα, Ca λ8542, and λ8662. The main shock continues to propagate outward and a Ca IR P Cygni profile could appear due to a radiative wake emission from the chromosphere (black arrow emitted by the green zone).

Table 2. Observational features of the Ca IR triplet in the star sample.

ϕ interval	Small ($P < 10$d)	Medium ($P \approx 10$d)	Long ($P > 10$d)
0.9–0.3	Quiescent profiles: The atmospheric layers are moving outward.	Quiescent profiles	Schwarzschild mechanism: Infalling chromosphere layers are collapsing onto the emerging shock causing a double absorption profile P Cygni profile: The main shock front is still propagating and progressively leaves Ca IR layers, entering in outermost Hα layers.
0.3–0.6	Quiescent profiles	Inverse P Cygni profile: Emission from supersonic infalling layers.	Quiescent profiles
0.6–1.0	Inverse P Cygni profile: A weak emission is observable in several short periods. Profile enlargement: The profiles are importantly wider due to turbulences during atmosphere collision.	Line doubling: Enlargement of the line profile which is possibly a double profile due to a Schwarzschild scenario.	P Cygni profile: It appears when the main shock from the previous cycle is high enough in the chromosphere. Inverse P Cygni profile: Emission from supersonic infalling layers. Transition phase: From 0.9 to 1.0 the latter emission progressively disappears. Schwarzschild mechanism initiates.

Notes. The table is divided into pulsation periods (columns) and phase interval (rows). In Fig. 6 we represent the mean features observed in each phase interval.

because of possible cycle-to-cycle variation effects (Anderson 2016), the Schwarzschild mechanism could be a common feature in long-period Cepheids.

The Schwarzschild mechanism itself occurs during the expansion of the Cepheids photosphere around $\phi = 0.9$. This is explained by a collision between the infalling layers of the lower chromosphere onto denser regions of the ascending photosphere. For each long-period Cepheid presenting double line features, we derive RVs from both blueshifted $V_{\rm blue}$ and redshifted $V_{\rm red}$ components using a bi-Gaussian fitting. We provide an example of this fitting in Fig. 9. From this fitting, we obtain both mean and standard deviation values of blue and red

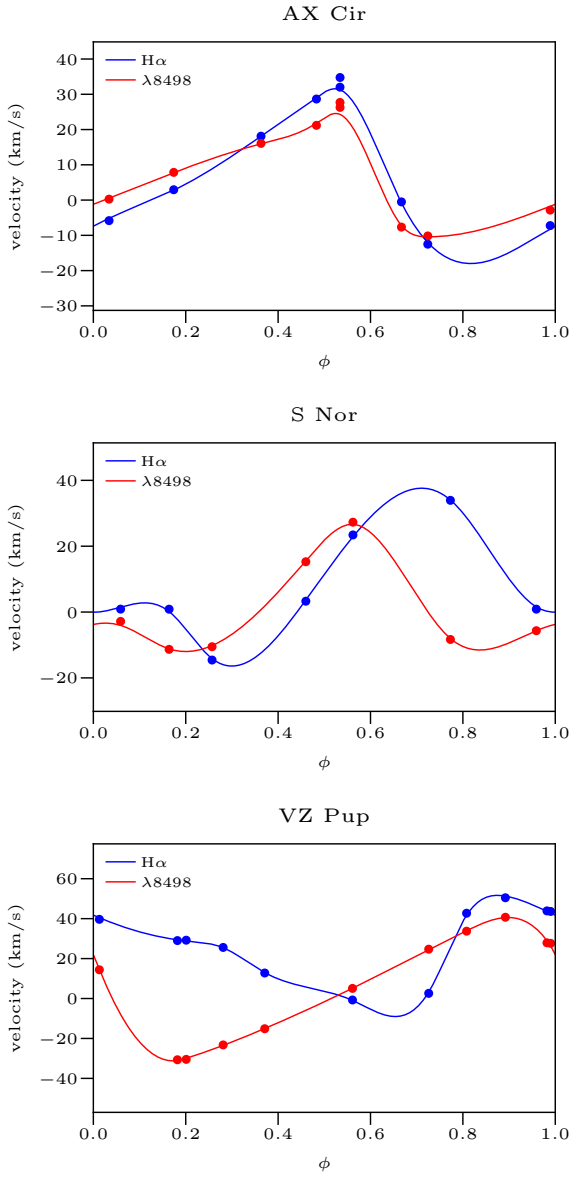

Fig. 7. Radial velocity of line Ca λ8498 and Hα line along the pulsation cycle ϕ for prototype stars. The solid curves are built from a spline fit to the RV data to guide the eye.

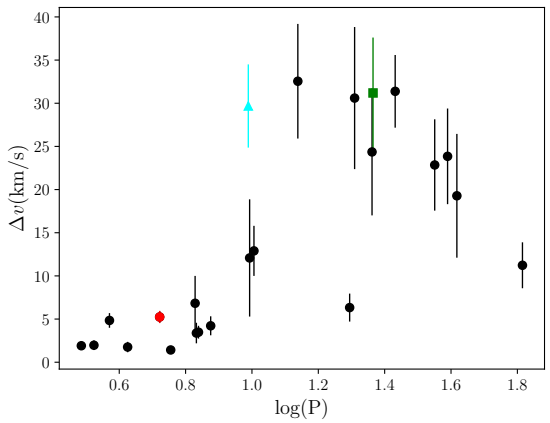

Fig. 8. Norm of the velocity gradient averaged over the pulsation cycle estimated using Eq. (1) vs. logarithm of the pulsation period. Red, cyan, and green marks are AX Cir, S Nor, and VZ Pup, respectively.

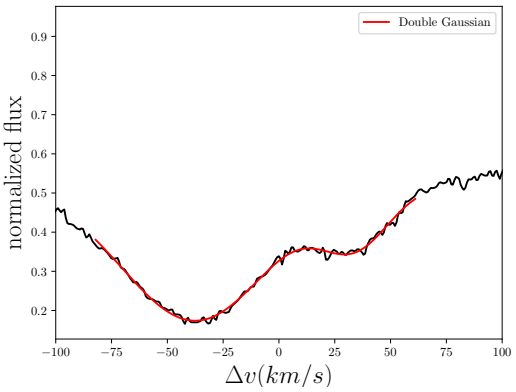

Fig. 9. Example of bi-Gaussian fit in the case of VZ Pup for line λ8542 at the pulsation phase $\phi = 0.08$. The parameters associated to the bi-Gaussian fits are listed for all stars in Table A.1, together with the derived shock amplitude.

absorption components. We also estimate the shock amplitude by simply assuming $A_{\rm shock} = V_{\rm red} - V_{\rm blue}$ and constant velocities during the infalling motion. Results are presented in Table A.1.

We obtain shock amplitudes between 50 and 80 km s^{-1}. Although these profiles belong to different pulsation phases, we observe no trend between the shock amplitude and the period of the Cepheids. In the case of VZ Pup the Schwarzschild mechanism is initiated at the end of the pulsation cycle ($\phi = 0.91$) for Ca λ8542 and λ8662. The double line feature disappears after $\phi = 0.179$. In that case, it took at least a quarter cycle ($\Delta\phi \approx 0.250$) for Ca λ8542 and λ8662 layers to collapse entirely on the photospheric denser region, resulting in a single blueshifted component. If we assume a constant shock amplitude during the collapsing of the chromosphere, we can approximate the maximum height of Ca λ8542 and λ8662 core formation regions. Indeed this is simply the atmosphere distance covered in a quarter period by the relative velocity of the collapsing layers $R_{\rm chromo} = P\Delta\phi A_{\rm shock}$. We therefore estimate this distance assuming $\Delta\phi = 0.250$ and using the shock amplitude from Ca λ8542 derived in Table A.1. In order to derive the chromospheric radius expressed by the mean stellar radius, we used the period–radius (PR) relation from Gallenne et al. (2017). Applying the same methodology for the long-period Cepheids in the sample, we find an extension for the chromosphere of Cepheids from about 40 to 50% of the mean stellar radius. The results are presented in Table 3. This order of magnitude is in agreement with that found by Wallerstein (1972), who estimated a Ca II fallen distance of 50% the radius of the star in the case of T Mon.

7. Discussion

7.1. Pulsating chromosphere as the origin of an ionized shell

A central question raised in Sect. 1 is whether or not the pulsating chromosphere has the potential to ionize the gas in the environment to produce an IR excess such as the one that would be caused by a shell of ionized gas, which represents 15% of the photosphere radius (Hocdé et al. 2020). In this paper, we studied the lower chromosphere of Cepheids for which we estimated a size of at least 50% of the star radius.

Several processes are able to provide ionized material in the lower chromosphere. We analyzed three episodes which have the potential to heat up and massively ionize the upper atmosphere: (1) the main shock travelling through the upper

Table 3. Chromospheric radius $R_{\rm chromo}$ estimated from shock amplitude listed in Table A.1 in the case of the calcium line λ8542.

Star	$A_{\rm shock}$ (km s^{-1})	R ($R_\odot$)	$R_{\rm chromo}$ (%R)
TT Aql	82.9 ± 1.1	82.0 ± 1.0	43.2 ± 1.1
RZ Vel	80.1 ± 1.3	107.4 ± 1.6	47.2 ± 1.5
WZ Car	83.2 ± 0.4	116.7 ± 1.8	50.9 ± 1.0
VZ Pup	69.3 ± 0.6	117.2 ± 1.8	42.5 ± 1.0
T Mon	82.4 ± 0.8	130.2 ± 2.2	53.1 ± 1.4
U Car	59.1 ± 0.4	167.0 ± 3.2	42.7 ± 1.1
RS Pup	81.3 ± 1.7	174.5 ± 3.5	60.0 ± 2.5
V1496 Aql	71.3 ± 3	238.3 ± 5.5	60.72 ± 4.0

Notes. $R_{\rm chromo}$ is given relative to the mean stellar radius provided by the PR relation from Gallenne et al. (2017). Calculation assumes $\Delta\phi = 0.250$ for Schwarzschild mechanism duration. Mean radius from PR relation: $\log R = (0.684 \pm 0.007)(\log P - 0.517) + (1.489 \pm 0.002)$.

atmosphere whose front amplitude can reach 100 km s^{-1}, (2) a shock caused by supersonic descending layers of the atmosphere revealed under the form of an inverse P Cygni profile, and (3) a Schwarzschild mechanism caused by the main shock which is reversing the movement of the descending layers of the atmosphere.

However, according to shock theory (Fokin et al. 2000, 2004), shocks alone seem unlikely to provide a permanent free–free continuum which could explain a constant IR excess. These authors have shown that cooling by FeI and FeII lines in the post-shock region is more effective than cooling by free-free and bound-free continuum. Moreover, these authors also estimated the size of the post-shock region to be about 100 km, and given that shock velocities are 10 to 100 km s^{-1} we deduce a cooling time of the order of tens of seconds which is short compared to a pulsation period.

In addition, the main shock traversing the photosphere rules a lot of processes in the behavior of Cepheids. Indeed, it is already hypersonic when it emerges from the surface of the star, with a shock velocity of about 100 km s^{-1} or more, which translates to a Mach number of between 10 and 20. In this case the convection zone could be strongly disrupted or inhibited at least for a fraction of the pulsation cycle.

We therefore propose that this shock could be strong enough to bring hot and dense material into the upper atmosphere. Interestingly, Kraft (1957) also suggested that the transitory development from Ca II K emission in classical Cepheids is associated with the presence of hot material low in the atmosphere. This latter authors further proposes that this material could have been convected upward from a hydrogen convection zone below the surface.

7.2. A plausible source of X-ray emission in the upper chromosphere

Another interesting question is to understand the origin of periodic X-ray emission around phase $\phi = 0.45$ at maximum radius observed by Engle et al. (2017). Such X-ray emission could stem from a high-temperature plasma in the higher chromosphere. Indeed at this phase, the shock is well detached from the photosphere. When the P Cygni appears in the Hα line at phase 0.0, the shock has already travelled ≈15% of the photospheric radius with a speed of 100 km s^{-1} or more. The shock then decelerates below 100 km s^{-1} around $\phi = 0.5$, and thus the shock is no longer able to produce hydrogen emission. At this time, the shock has travelled a distance close to the photospheric radius and is now propagating in the upper atmosphere where the density is three or four orders of magnitude weaker (10^{-11}–10^{-12} g cm^{-3}) than that in the photosphere (10^{-8} g cm^{-3}). In this case, according to Fadeyev & Gillet (2004), with such a pre-shock density in the upper atmosphere, the thickness of the radiative wake increases by almost three orders of magnitude while the temperature just after the shock front changes relatively little. Part of the thickness of the radiative shell will be a few hundreds or at least thousands of kilometers. The plasma behind the shock is also strongly compressed, proportional to the square of the Mach number (given by the Hugoniot-Rankine equation in isothermal condition), and so is the amplification rate of the magnetic field, preexisting or generated by the plasma of the radiative wake, which may easily reach a factor of 100. Therefore, in the upper chromosphere, part of the energy dissipation of the shock may be in noncollisional form. As a conclusion, we suggest that the energy-producing X-ray flux between $\phi \approx 0.4$ and 0.5 could be deposited by the main shock in the outermost layers of the chromosphere.

7.3. Is the Gaia RVS sensitive to the chromosphere dynamics?

The *Gaia* RVS has a narrow wavelength range centered on the Ca IR triplet (from ~845 to ~872 nm, see Sartoretti et al. 2018). Therefore, we expect the RV time series produced by the RVS to be dependent on the Ca IR behavior. From the chromosphere kinematics using the Van Hoof effect in Sect. 5, we show that Hα lines are de-synchronized with an important velocity gradient compared to Ca IR for Cepheids with pulsation periods larger than about 10d. We therefore suggest that the same tendency as seen in Fig. 8 could appear between metallic lines (which are formed at a great optical depth) and Ca IR when observing with the RVS instrument. This de-synchronization between metallic and Ca IR lines was already observed by Wallerstein et al. (2015, 2019) for Cepheids δ Cep and X Cyg. Further investigations are necessary to quantify these differences and calibrate, if necessary, the projection factor to be used together with the RVS measurements of Cepheid RVs in the Baade-Wesselink method of distance determination (Nardetto et al. 2017).

8. Conclusion

We analyzed Hα and Ca IR profile variations to qualitatively describe the chromosphere dynamics over the pulsation period based on a sample of 24 stars with a good period coverage from short- up to long-period Cepheids. We demonstrate that Ca IR are interesting lines for probing dynamics in the lower chromosphere of Cepheids, and that they are complementary to Hα lines because their cores probe different heights in the atmospheric layers and can be used as unambiguous indicators of chromospheric activity. Our analysis leads to the following conclusions:

1. We confirm the Hα profile variation model made by Gillet (2014) in the particular case of X Cygni for a wider sample of long-period Cepheids.
2. As found by Nardetto et al. (2008), in the case of ℓ Car, we identify a Hα absorption feature centered on 0 km s^{-1} in at least eight long-period Cepheids (TT Aql, RZ Vel, WZ Car, VZ Pup, T Mon, ℓ Car, U Car, RS Pup), which we interpret as a static CSE that obscures the chromosphere and the star. Since the calcium abundance is lower than that of hydrogen,

we expect that the CSE absorption is weaker in Ca IR compared to Hα. However, we do not exclude a possible blend of the calcium emission if the CSE is denser in some cases.

3. We demonstrate that at least two mechanisms are pulsationally activating the chromosphere owing to the Ca IR diagnostic: (1) an inverse P Cygni profile emission during supersonic infalling motion and (2) a P Cygni profile emission due to the radiative wake behind the main shock when it is sufficiently detached from the photosphere. In addition, blended emission during the Schwarzschild mechanism, due to large amounts of kinetic energy released when the main shock and the infalling atmosphere are colliding, is also not excluded.
4. The difference in height formation of Ca IR and Hα creates a de-synchronization of their associated chromospheric layers due to an outward propagation wave. We observe a weak phase delay and velocity gradient ($\Delta v < 5$ km s^{-1}) in short-period Cepheids ($P < 10$ days) while Hα lines are delayed with an important velocity gradient (up to $\Delta v \approx 30$ km s^{-1}) compared to Ca IR in medium- and long-period Cepheids.
5. This de-synchronization in long-period Cepheids is likely responsible for the Schwarzschild mechanism of Ca IR lines during the beginning of the photosphere ascending phase from $\phi = 0.9$ to 0.3. This phenomenon is possibly a common feature since we observed it among eight out of ten cases of long-period Cepheids. The collision velocity between infalling layers of the lower part of the atmosphere and the photospheric region is about 50 up to 80 km s^{-1}. Since the infalling motion lasts for at least a quarter cycle we derived the height of Ca IR core formation to be ≈50% of the star radius in long-period Cepheids, which is consistent at first order with the size of the shell of ionized gas (15% of the stellar radius) found by Hocdé et al. (2020).

Further observations with a better pulsation cycle coverage are still needed to describe the chromosphere dynamics of short-, medium-, and long-period Cepheids. This could be a key to unbias PL relation from Cepheids IR excess.

Acknowledgements. The authors acknowledge the support of the French Agence Nationale de la Recherche (ANR), under grant ANR-15-CE31-0012- 01 (project UnlockCepheids). We acknowledge financial support from "Programme National de Physique Stellaire" (PNPS) of CNRS/INSU, France. This project was partially supported by the Polish Ministry of Science grant Ideas Plus. This research made use of the SIMBAD and VIZIER (http://cdsweb.u-strasbg.fr/) databases at CDS, Strasbourg (France) and the electronic bibliography maintained by the NASA/ADS system. This research also made use of Astropy, a community-developed core Python package for Astronomy (Astropy Collaboration 2018). This research has made use of the SIMBAD database, operated at CDS, Strasbourg, France. Based on observations made with ESO telescopes at Paranal La Silla observatories under program IDs: 098.D-0379(A), 0100.D-0397(A) and 0101.D-0551(A).

References

Anderson, R. I. 2016, MNRAS, 463, 1707
Astropy Collaboration (Price-Whelan, A. M., et al.) 2018, AJ, 156, 123
Baldry, I. K., Taylor, M. M., Bedding, T. R., & Booth, A. J. 1997, MNRAS, 289, 979
Bell, R. A., & Rodgers, A. W. 1967, MNRAS, 135, 121
Berdnikov, L. N., Samus, N. N., Antipin, S. V., et al. 2004, PASP, 116, 536
Bohm-Vitense, E., & Parsons, S. B. 1983, ApJ, 266, 171
Borgniet, S., Kervella, P., Nardetto, N., et al. 2019, A&A, 631, A37
Breitfellner, M. G., & Gillet, D. 1993a, A&A, 277, 524
Breitfellner, M. G., & Gillet, D. 1993b, A&A, 277, 553
Breitfellner, M. G., & Gillet, D. 1993c, A&A, 277, 541
Breitfelder, J., Mérand, A., Kervella, P., et al. 2016, A&A, 587, A117
Busà, I., Aznar Cuadrado, R., Terranegra, L., Andretta, V., & Gomez, M. T. 2007, A&A, 466, 1089
Cauzzi, G., Reardon, K. P., Uitenbroek, H., et al. 2008, A&A, 480, 515
Cauzzi, G., Reardon, K., Rutten, R. J., Tritschler, A., & Uitenbroek, H. 2009, A&A, 503, 577
Chmielewski, Y. 2000, A&A, 353, 666
Dekker, H., D'Odorico, S., Kaufer, A., Delabre, B., & Kotzlowski, H. 2000, Proc. SPIE, 4008, 534
Engle, S. G., Guinan, E. F., Harper, G. M., et al. 2017, ApJ, 838, 67
Fadeyev, Y. A., & Gillet, D. 2004, A&A, 420, 423
Foing, B. H., Crivellari, L., Vladilo, G., Rebolo, R., & Beckman, J. E. 1989, A&AS, 80, 189
Fokin, A. B. 1991, MNRAS, 250, 258
Fokin, A. B., Gillet, D., & Breitfellner, M. G. 1996, A&A, 307, 503
Fokin, A., Massacrier, G., & Gillet, D. 2000, A&A, 355, 668
Fokin, A. B., Massacrier, G., & Gillet, D. 2004, A&A, 420, 1047
Gaia Collaboration 2018, VizieR Online Data Catalog: I/345
Gallenne, A., Kervella, P., & Mérand, A. 2012, A&A, 538, A24
Gallenne, A., Mérand, A., Kervella, P., et al. 2013, A&A, 558, A140
Gallenne, A., Kervella, P., Mérand, A., et al. 2017, A&A, 608, A18
Gillet, D. 2014, A&A, 568, A72
Gontcharov, G. A. 2006, Astron. Lett., 32, 759
Groenewegen, M. A. T. 2020, A&A, 635, A33
Hertzsprung, E. 1926, Bull. Astron. Inst. Netherlands, 3, 115
Hocdé, V., Nardetto, N., Lagadec, E., et al. 2020, A&A, 633, A47
Hubble, E. P. 1926, ApJ, 64, 321
Hubble, E. 1929, Proc. Natl. Acad. Sci., 15, 168
Jacobsen, T. S., & Wallerstein, G. 1981, PASP, 93, 481
Jacobsen, T. S., & Wallerstein, G. 1982, PASP, 94, 471
Katz, D., Sartoretti, P., Cropper, M., et al. 2019, A&A, 622, A205
Kervella, P., Mérand, A., Perrin, G., & Coudé du Foresto, V. 2006, A&A, 448, 623
Kervella, P., Trahin, B., Bond, H. E., et al. 2017, A&A, 600, A127
Kovacs, G., Kisvarsanyi, E. G., & Buchler, J. R. 1990, ApJ, 351, 606
Kovtyukh, V. V., Wallerstein, G., Andrievsky, S. M., et al. 2011, A&A, 526, A116
Kraft, R. P. 1957, ApJ, 125, 336
Leavitt, H. S. 1908, Ann. Harvard College Observ., 60, 87
Linsky, J. L., Teske, R. G., & Wilkinson, C. W. 1970, Sol. Phys., 11, 374
Linsky, J. L., Hunten, D. M., Sowell, R., Glackin, D. L., & Kelch, W. L. 1979, ApJS, 41, 481
Martin, J., Fuhrmeister, B., Mittag, M., et al. 2017, A&A, 605, A113
Mathias, P., & Gillet, D. 1993, A&A, 278, 511
Mérand, A., Kervella, P., Coudé du Foresto, V., et al. 2006, A&A, 453, 155
Mérand, A., Kervella, P., Breitfelder, J., et al. 2015, A&A, 584, A80
Mermilliod, J. C., Mayor, M., & Udry, S. 2008, A&A, 485, 303
Munari, U. 1999, Balt. Astron., 8, 73
Nardetto, N., Groh, J. H., Kraus, S., Millour, F., & Gillet, D. 2008, A&A, 489, 1263
Nardetto, N., Poretti, E., Rainer, M., et al. 2017, A&A, 597, A73
Pourbaix, D., Tokovinin, A. A., Batten, A. H., et al. 2004, A&A, 424, 727
Reardon, K. P., Uitenbroek, H., & Cauzzi, G. 2009, A&A, 500, 1239
Riess, A. G., Filippenko, A. V., Challis, P., et al. 1998, AJ, 116, 1009
Riess, A. G., Casertano, S., Yuan, W., Macri, L. M., & Scolnic, D. 2019, ApJ, 876, 85
Rodgers, A. W., & Bell, R. A. 1968, MNRAS, 138, 23
Samus', N. N., Kazarovets, E. V., Durlevich, O. V., Kireeva, N. N., & Pastukhova, E. N. 2017, Astron. Rep., 61, 80
Sartoretti, P., Katz, D., Cropper, M., et al. 2018, A&A, 616, A6
Sasselov, D. D., & Lester, J. B. 1994a, ApJ, 423, 785
Sasselov, D. D., & Lester, J. B. 1994c, ApJ, 423, 795
Sasselov, D. D., & Lester, J. B. 1994b, ApJ, 423, 777
Schmidt, E. G. 1970, ApJ, 162, 871
Schmidt, E. G. 2015, ApJ, 813, 29
Schmidt, E. G., & Parsons, S. B. 1982, ApJS, 48, 185
Schmidt, E. G., & Parsons, S. B. 1984, ApJ, 279, 202
Schmidt, E. G., & Weiler, E. J. 1979, AJ, 84, 231
Schwarzschild, M. 1952, Transactions of the IAU, Vol. VIII, ed. P. T., Oosterhoff (Cambridge: Cambridge University Press), 81
Turner, D. G., Abdel-Sabour Abdel-Latif, M., & Berdnikov, L. N. 2006, PASP, 118, 410
van Hoof, A., & Struve, O. 1953, PASP, 65, 158
Vecchio, A., Cauzzi, G., & Reardon, K. P. 2009, A&A, 494, 269
Vernazza, J. E., Avrett, E. H., & Loeser, R. 1973, ApJ, 184, 605
Wallerstein, G. 1972, PASP, 84, 656
Wallerstein, G., Albright, M. B., & Ritchey, A. M. 2015, PASP, 127, 503
Wallerstein, G., Anderson, R. I., Farrell, E. M., et al. 2019, PASP, 131, 094203
Watson, C. L., Henden, A. A., & Price, A. 2006, Soc. Astron. Sci. Ann. Symp., 25, 47
Wilson, O. C., & Vainu Bappu, M. K. 1957, ApJ, 125, 661

Appendix A: Results of bi-Gaussian fitting for Schwarzschild mechanism

Table A.1. Radial-velocity fields in Schwarzschild mechanism in long-period Cepheids.

Star	Phase	Line	$V_{\rm blue}$	$V_{\rm red}$	$A_{\rm shock}$	$\sigma_{\rm blue}$	$\sigma_{\rm red}$
TT Aql	0.947	2	-36.7 ± 1.0	$+46.2 \pm 0.5$	82.9 ± 1.1	42.8 ± 0.9	31.6 ± 0.7
		3	-29.7 ± 0.7	$+47.4 \pm 0.6$	77.1 ± 0.9	42.5 ± 0.7	29.2 ± 0.6
	0.116	2	-35.5 ± 0.1	$+41.7 \pm 0.7$	77.2 ± 0.7	41.4 ± 0.7	15.1 ± 0.8
		3	-31.6 ± 0.1	$+44.7 \pm 1.2$	76.3 ± 1.2	36.1 ± 0.9	14.2 ± 1.4
RZ Vel	0.955	2	-43.3 ± 1.2	$+36.8 \pm 0.6$	80.1 ± 1.3	35.0 ± 0.8	18.5 ± 0.6
		3	-40.0 ± 0.1	$+39.1 \pm 0.4$	79.1 ± 0.4	33.6 ± 0.2	20.4 ± 0.4
WZ Car	0.080	1	-43.0 ± 0.1	$+39.3 \pm 0.7$	82.3 ± 0.7	36.3 ± 0.1	21.7 ± 0.6
		2	-48.2 ± 0.2	$+35.0 \pm 0.4$	83.2 ± 0.4	34.3 ± 0.8	31.6 ± 0.4
		3	-46.2 ± 0.1	$+34.5 \pm 0.2$	80.7 ± 0.2	29.6 ± 0.4	19.8 ± 0.3
VZ Pup	0.080	2	-37.3 ± 0.1	$+32.0 \pm 0.6$	69.3 ± 0.6	29.8 ± 0.7	14.0 ± 0.8
		3	-34.2 ± 0.1	$+33.6 \pm 1.1$	67.8 ± 1.1	28.5 ± 0.3	14.2 ± 0.5
	0.179	2	-28.9 ± 0.1	$+32.3 \pm 0.4$	61.2 ± 0.4	29.4 ± 0.3	10.5 ± 0.5
		3	-26.6 ± 0.1	$+37.2 \pm 0.4$	63.8 ± 0.4	28.0 ± 0.2	11.0 ± 0.5
T Mon	0.123	1	-41.6 ± 0.1	$+28.2 \pm 0.7$	69.8 ± 0.8	35.7 ± 1.1	16.0 ± 0.5
		2	-49.4 ± 0.2	$+33.0 \pm 0.8$	82.4 ± 0.8	47.5 ± 2.0	22.5 ± 0.6
		3	-45.8 ± 0.1	$+28.6 \pm 0.1$	74.4 ± 0.1	36.0 ± 0.3	17.4 ± 0.1
U Car	0.197	2	-30.9 ± 0.1	$+28.2 \pm 0.1$	59.1 ± 0.4	30.1 ± 0.5	17.3 ± 0.5
		3	-26.8 ± 0.1	$+41.5 \pm 2.9$	68.3 ± 2.9	20.3 ± 0.3	6.5 ± 1.6
	0.225	2	-27.1 ± 0.2	$+33.6 \pm 1.6$	60.7 ± 1.6	37.0 ± 1.2	16.5 ± 0.5
		3	-24.5 ± 0.2	$+40.6 \pm 0.1$	65.1 ± 0.2	37.8 ± 2.3	18.0 ± 0.9
RS Pup	0.280	1	-33.6 ± 0.1	$+30.4 \pm 0.7$	64.0 ± 0.7	33.1 ± 1.3	14.8 ± 0.5
		2	-41.1 ± 1.0	$+40.2 \pm 1.4$	81.3 ± 1.7	54.1 ± 3.6	26.4 ± 1.8
		3	-36.1 ± 0.9	$+35.9 \pm 0.7$	72.0 ± 1.1	44.0 ± 1.5	20.2 ± 0.4
V1496 Aql	0.625	1	-20.7 ± 0.3	$+28.5 \pm 0.3$	49.2 ± 0.4	17.2 ± 0.4	21.6 ± 0.3
		2	-38.5 ± 1.2	$+32.8 \pm 0.4$	71.3 ± 1.3	28.1 ± 0.6	32.5 ± 1.2
		3	-27.2 ± 0.7	$+33.4 \pm 0.4$	60.6 ± 0.8	26.2 ± 0.8	24.9 ± 0.6

Notes. Velocities were calculated only when the characteristic W-shape was clearly identified by eye. In the third column of the table, lines 1, 2 and 3 refer to Ca λ8498, 8542 and 8662, respectively. $V_{\rm blue}$, $V_{\rm red}$ are the blue and the red component velocities respectively of the W shape. $A_{\rm shock}$ is the shock amplitude derived by $V_{\rm blue}-V_{\rm red}$. The FWHM of blue ($\sigma_{\rm blue}$) and red ($\sigma_{\rm red}$) components are also listed. All values are given in (km s^{-1}). Stars are ranged by increasing periods from top to bottom.

Appendix B: Calcium triplet of Cepheids with UVES

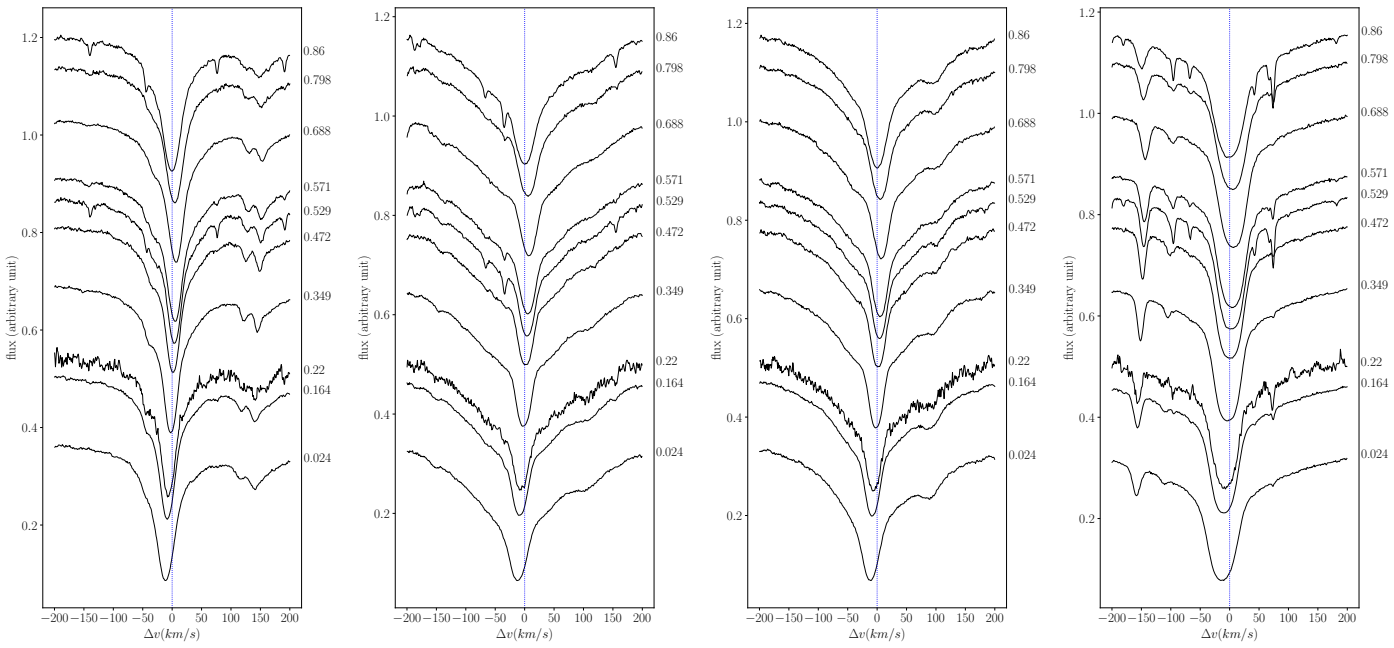

(a) λ8498 (b) λ8542 (c) λ8662 (d) Hα

Fig. B.1. AV Cir, 3.06 d.

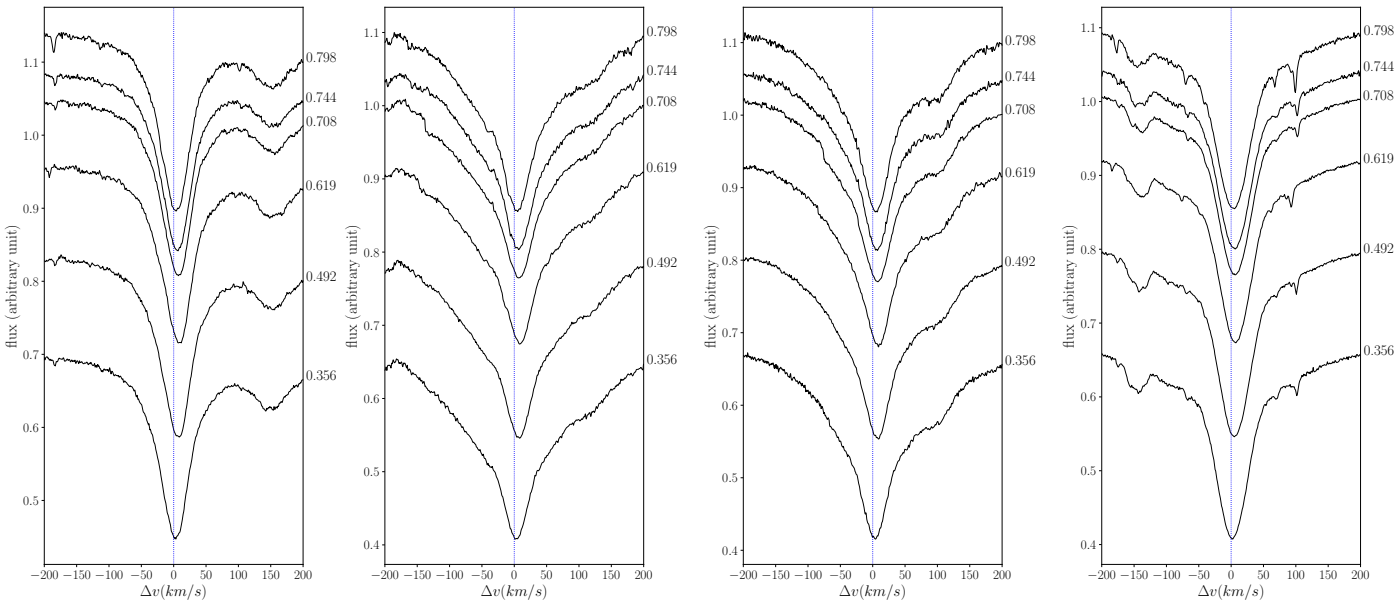

(a) λ8498 (b) λ8542 (c) λ8662 (d) Hα

Fig. B.2. BG Cru, 3.34 d.

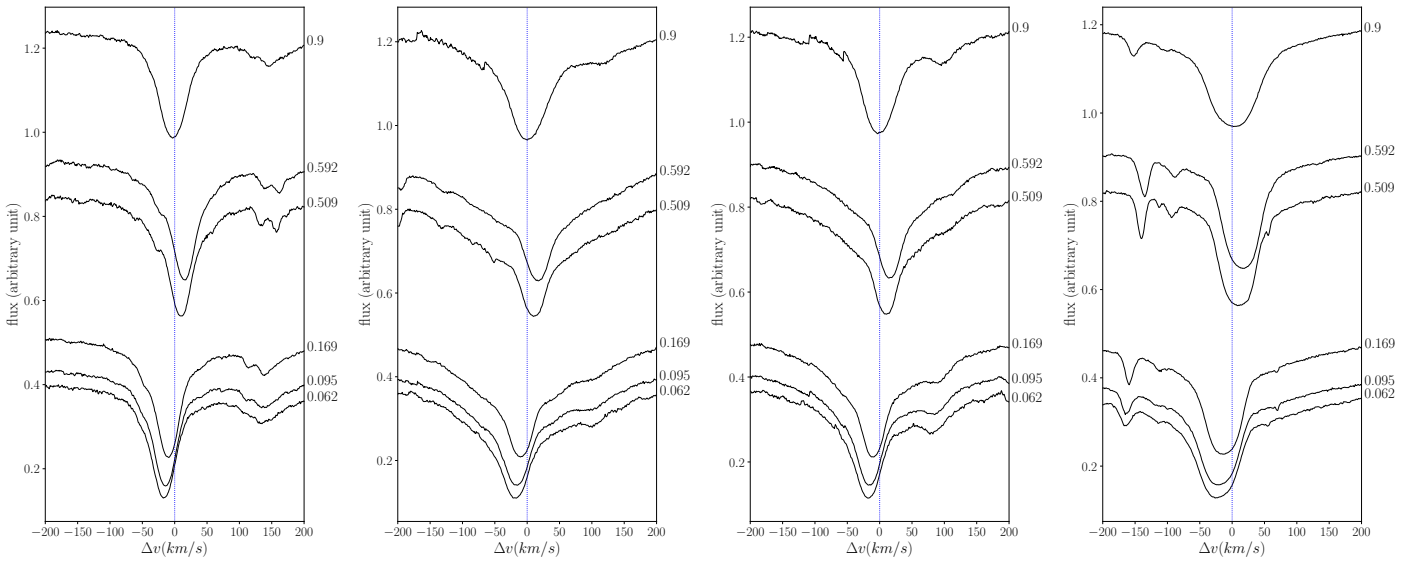

(a) λ8498 (b) λ8542 (c) λ8662 (d) Hα

Fig. B.3. RT Aur, 3.74 d.

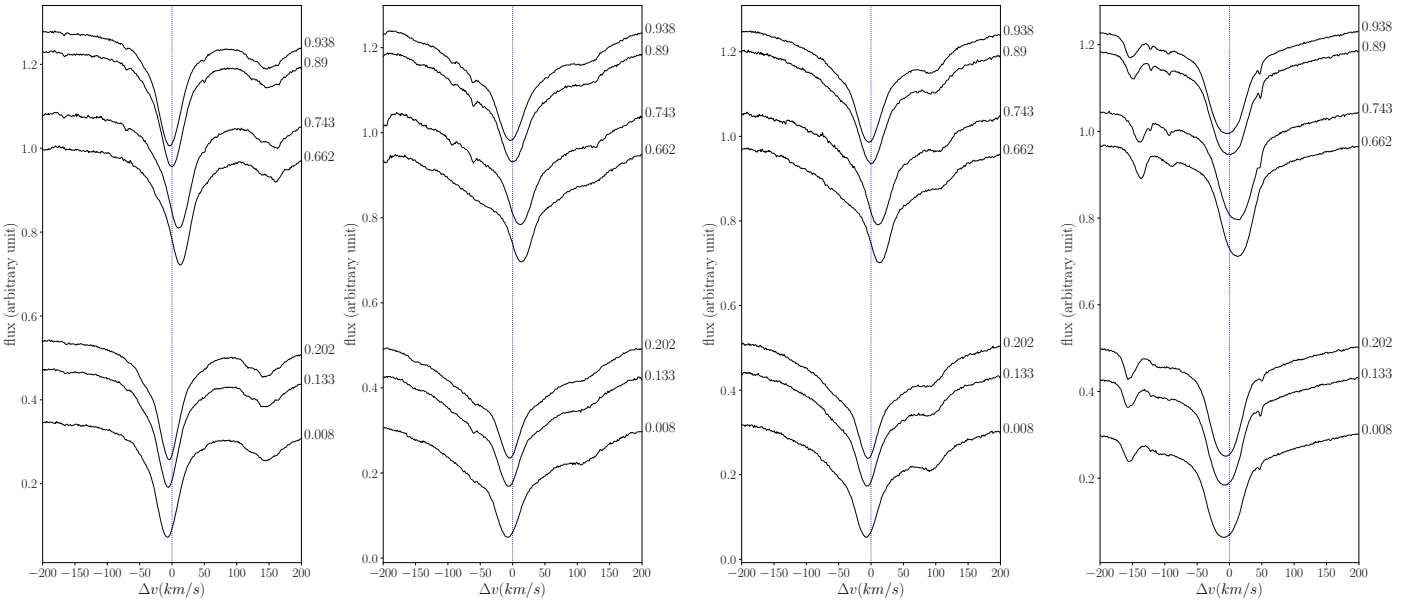

(a) λ8498 (b) λ8542 (c) λ8662 (d) Hα

Fig. B.4. AH Vel, 4.22 d.

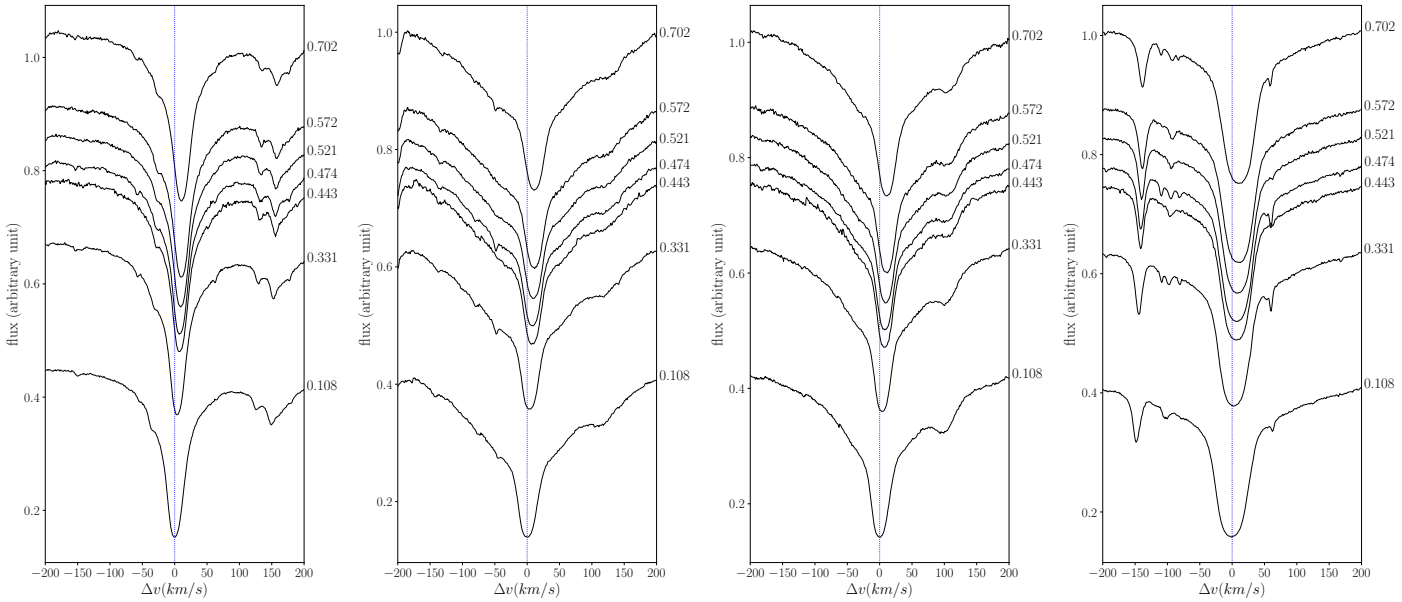

(a) λ8498 (b) λ8542 (c) λ8662 (d) Hα

Fig. B.5. MY Pup, 5.69 d.

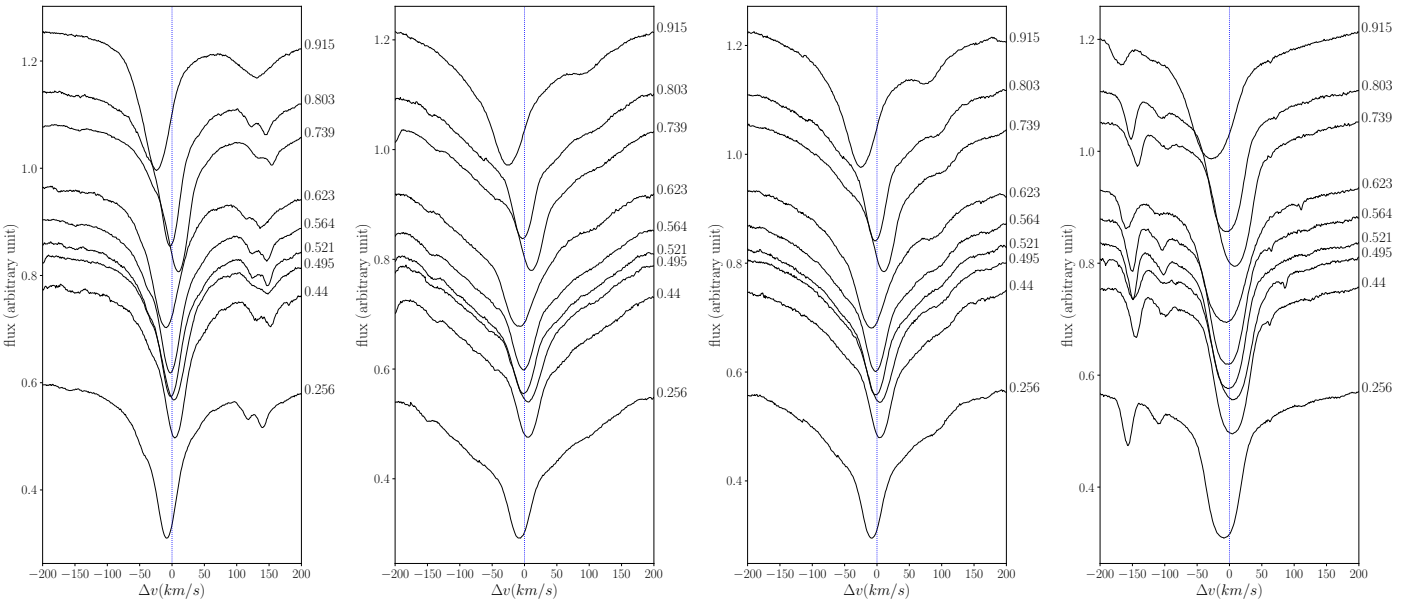

(a) λ8498 (b) λ8542 (c) λ8662 (d) Hα

Fig. B.6. EW Sct, 5.82 d.

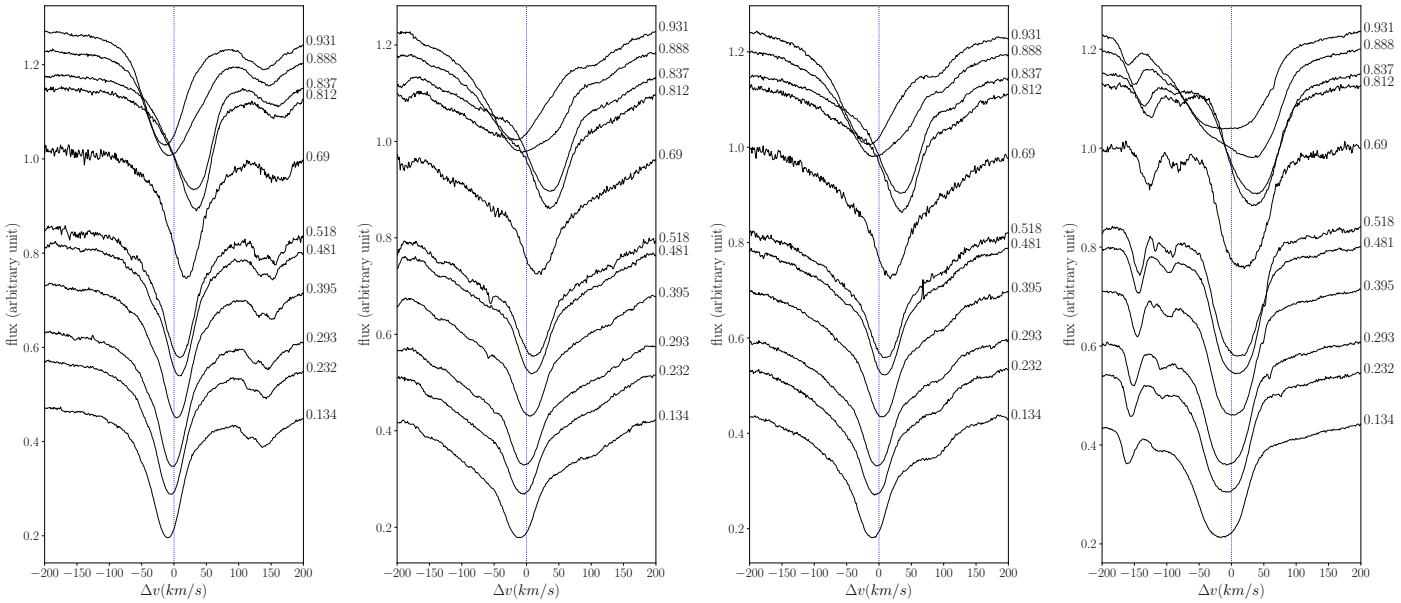

(a) λ8498 (b) λ8542 (c) λ8662 (d) Hα

Fig. B.7. U Sgr, 6.75 d.

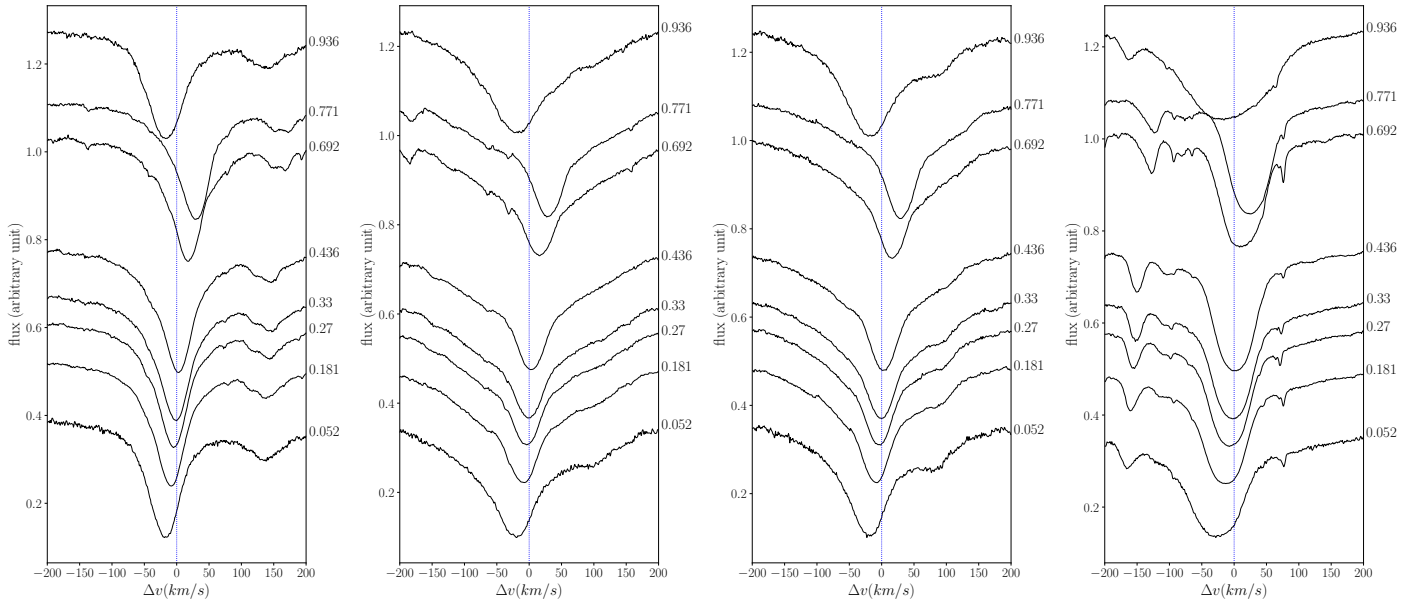

(a) λ8498 (b) λ8542 (c) λ8662 (d) Hα

Fig. B.8. R Mus, 7.51 d.

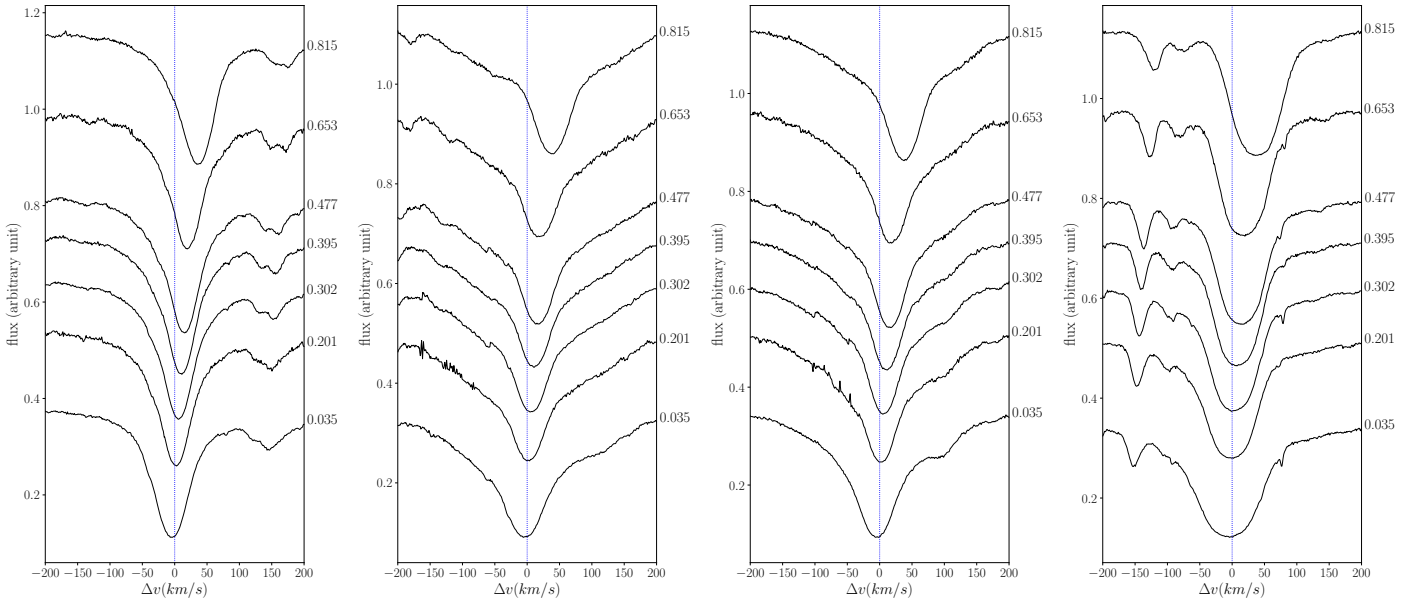

(a) λ8498 (b) λ8542 (c) λ8662 (d) Hα

Fig. B.9. V636 Sco, 7.8 d.

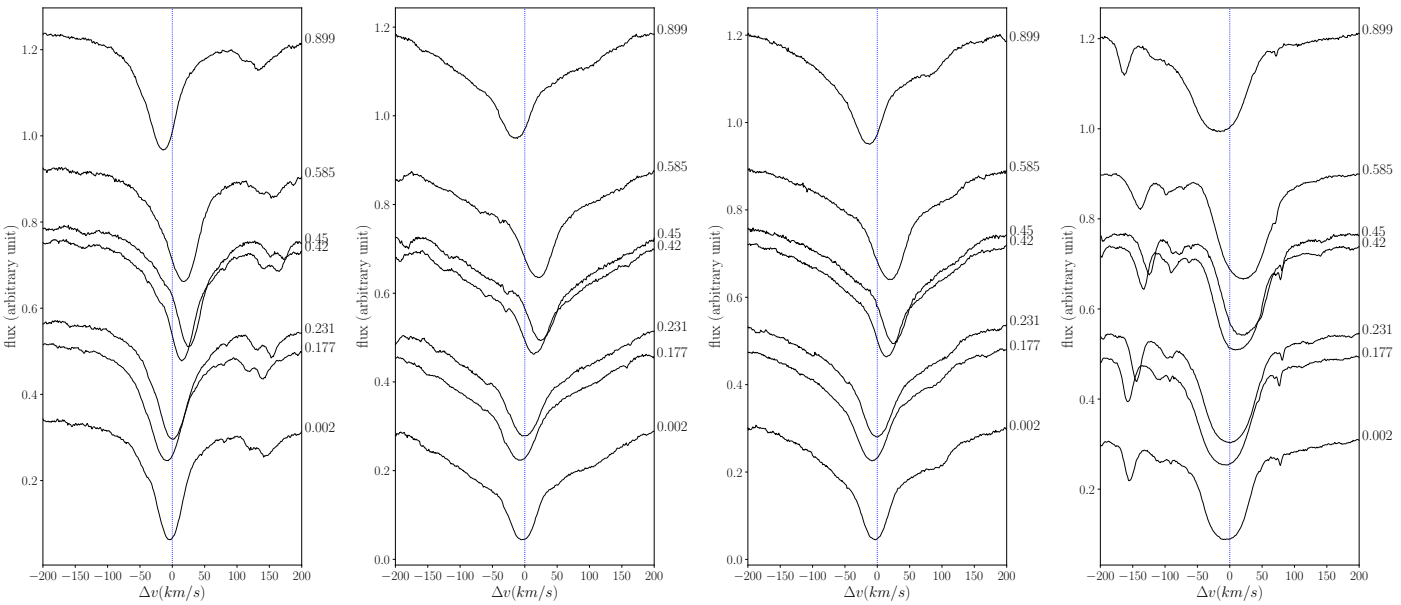

(a) λ8498 (b) λ8542 (c) λ8662 (d) Hα

Fig. B.10. S Mus, 9.66 d.

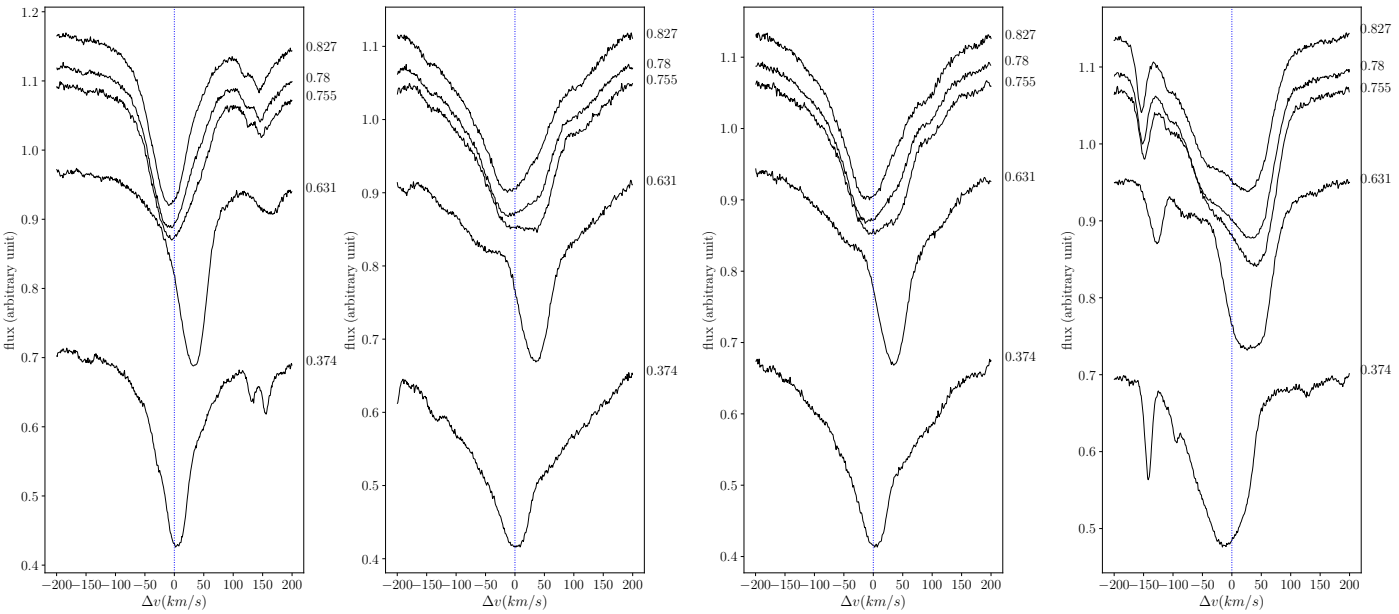

(a) λ8498 (b) λ8542 (c) λ8662 (d) Hα

Fig. B.11. β Dor, 9.84 d.

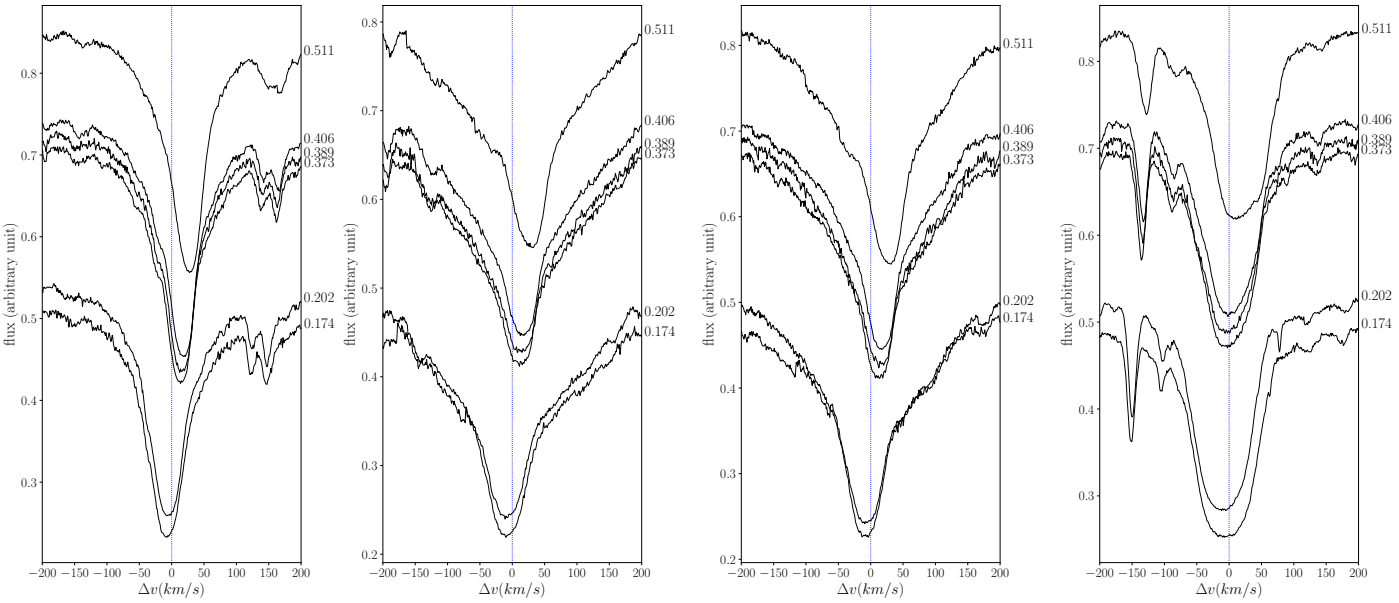

(a) λ8498 (b) λ8542 (c) λ8662 (d) Hα

Fig. B.12. ζ Gem, 10.15 d.

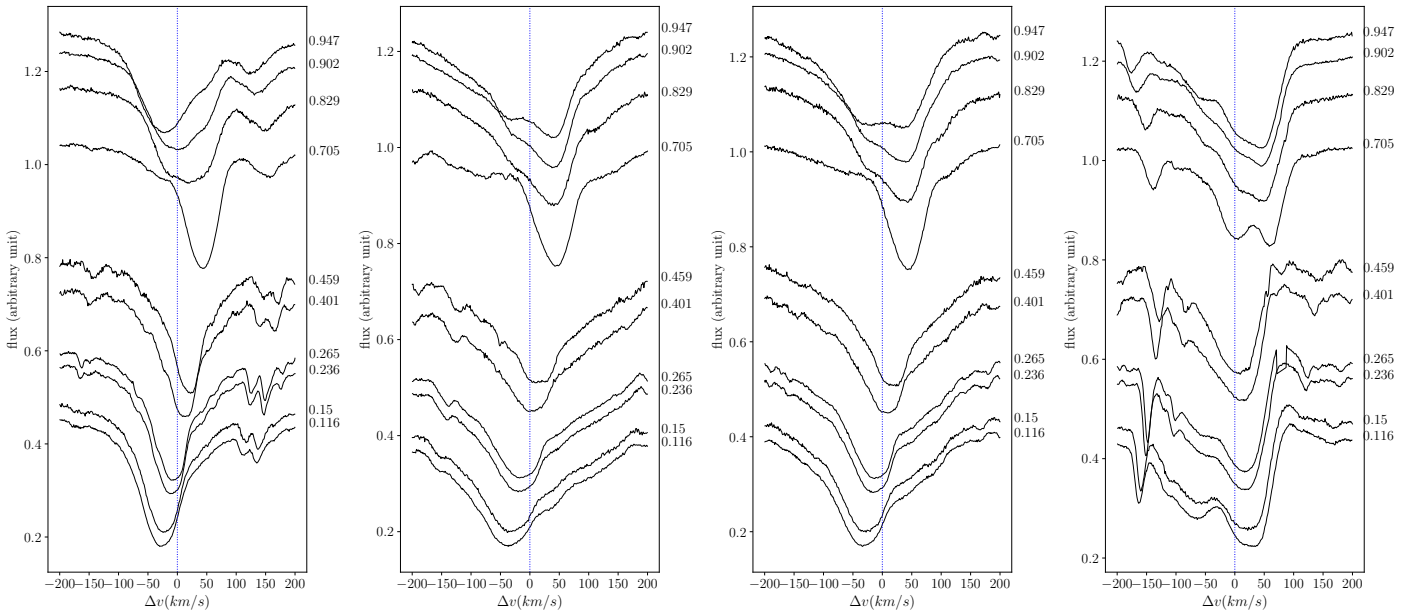

(a) λ8498 (b) λ8542 (c) λ8662 (d) Hα

Fig. B.13. TT Aql, 13.75 d.

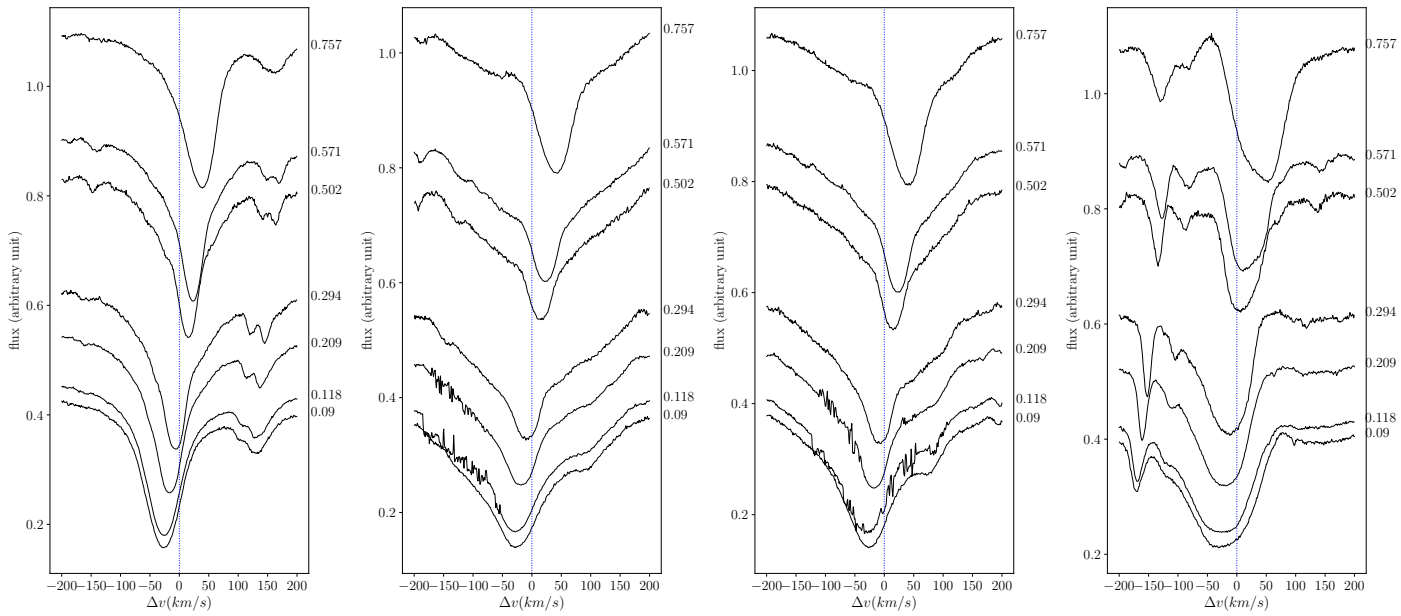

(a) λ8498 (b) λ8542 (c) λ8662 (d) Hα

Fig. B.14. RU Sct, 19.70 d.

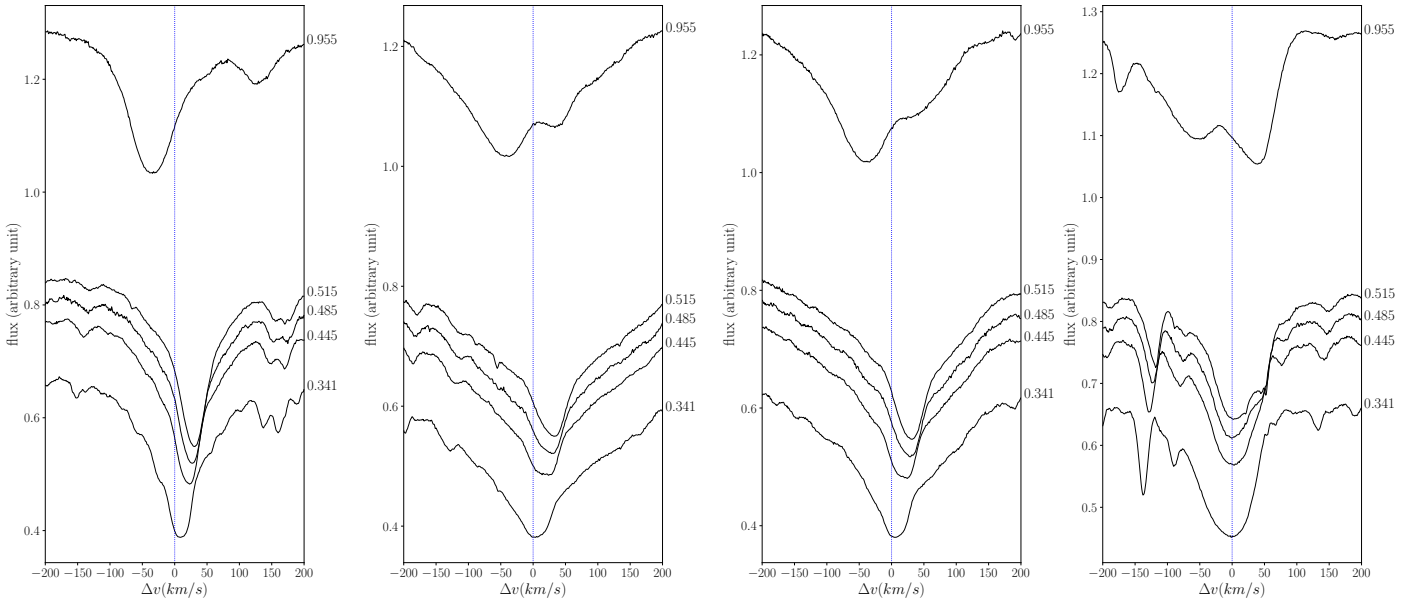

(a) λ8498 (b) λ8542 (c) λ8662 (d) Hα

Fig. B.15. RZ Vel, 20.39 d.

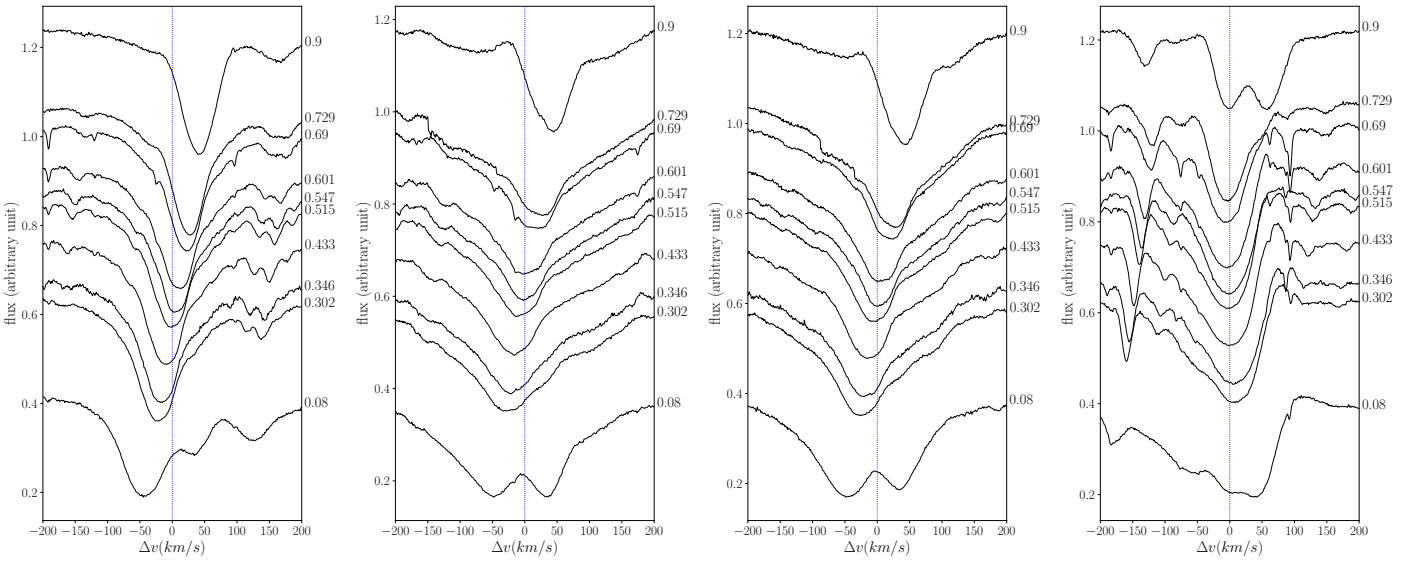

(a) λ8498 (b) λ8542 (c) λ8662 (d) Hα

Fig. B.16. WZ Car, 23.01 d.

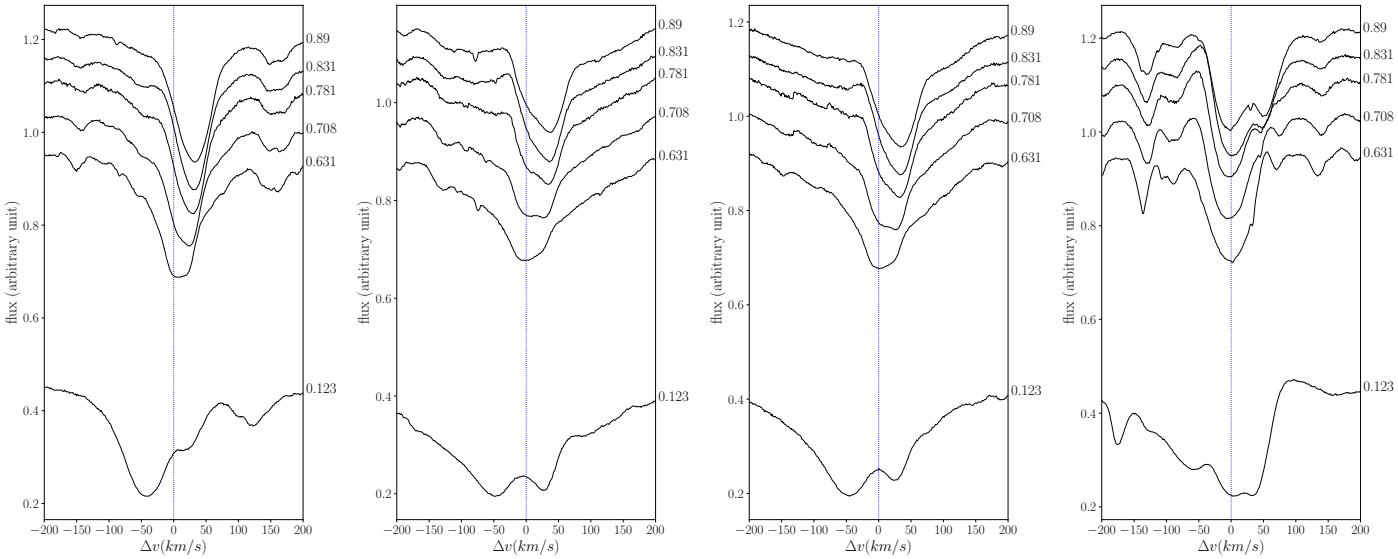

(a) λ8498 (b) λ8542 (c) λ8662 (d) Hα

Fig. B.17. T Mon, 27.02 d.

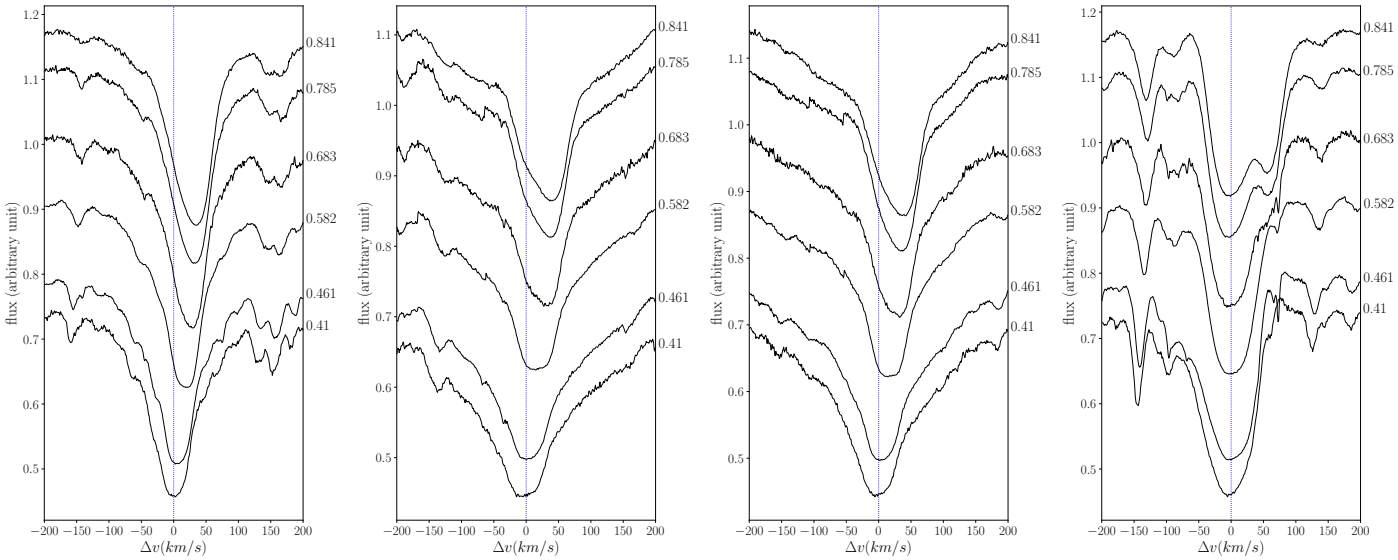

(a) λ8498 (b) λ8542 (c) λ8662 (d) Hα

Fig. B.18. ℓ Car, 35.55 d.

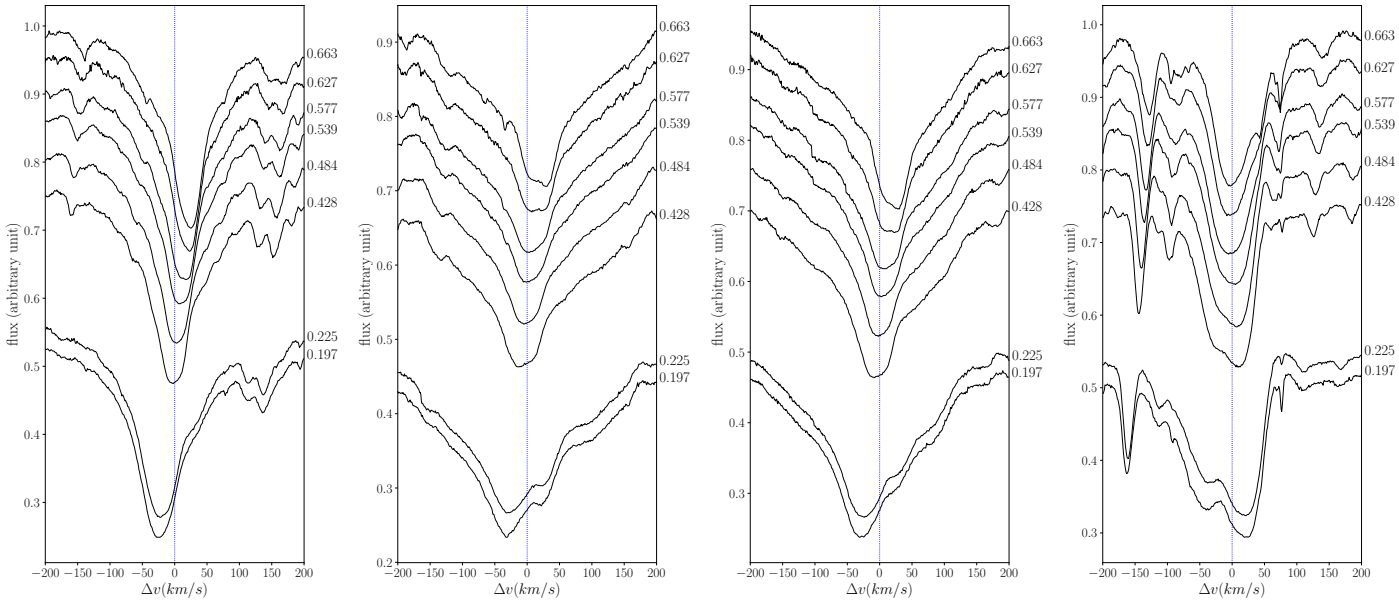

(a) λ8498 (b) λ8542 (c) λ8662 (d) Hα

Fig. B.19. U Car, 38.80 d.

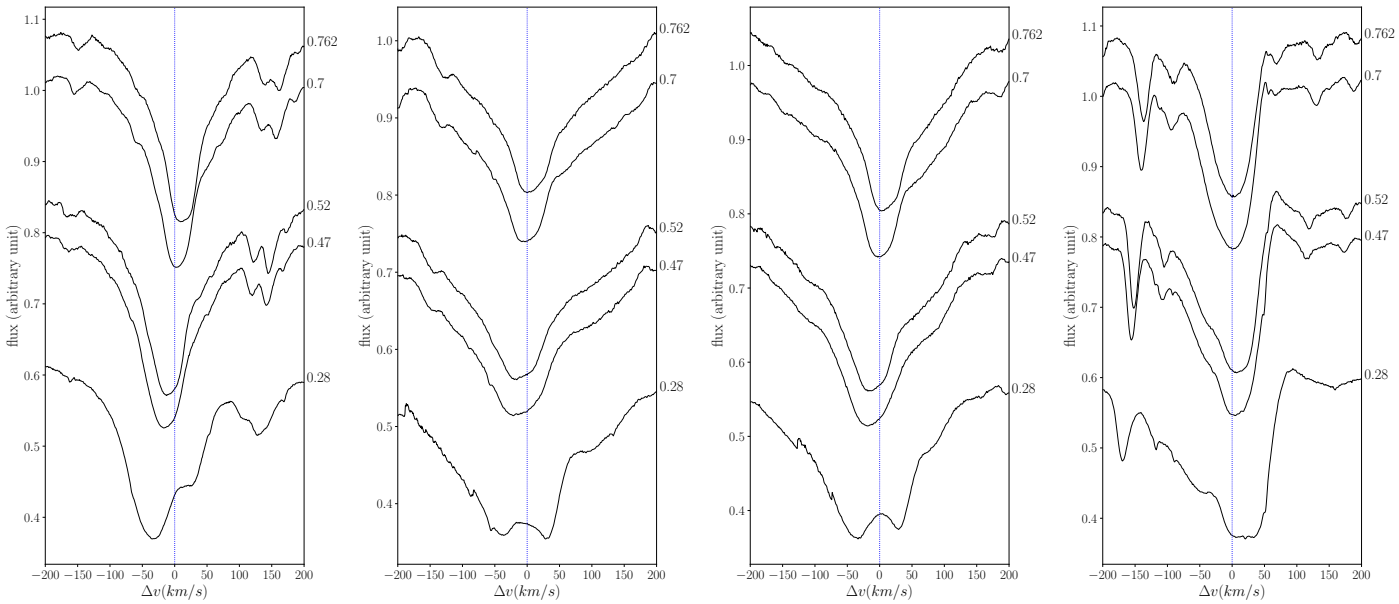

(a) λ8498 (b) λ8542 (c) λ8662 (d) Hα

Fig. B.20. RS Pup, 41.46 d.

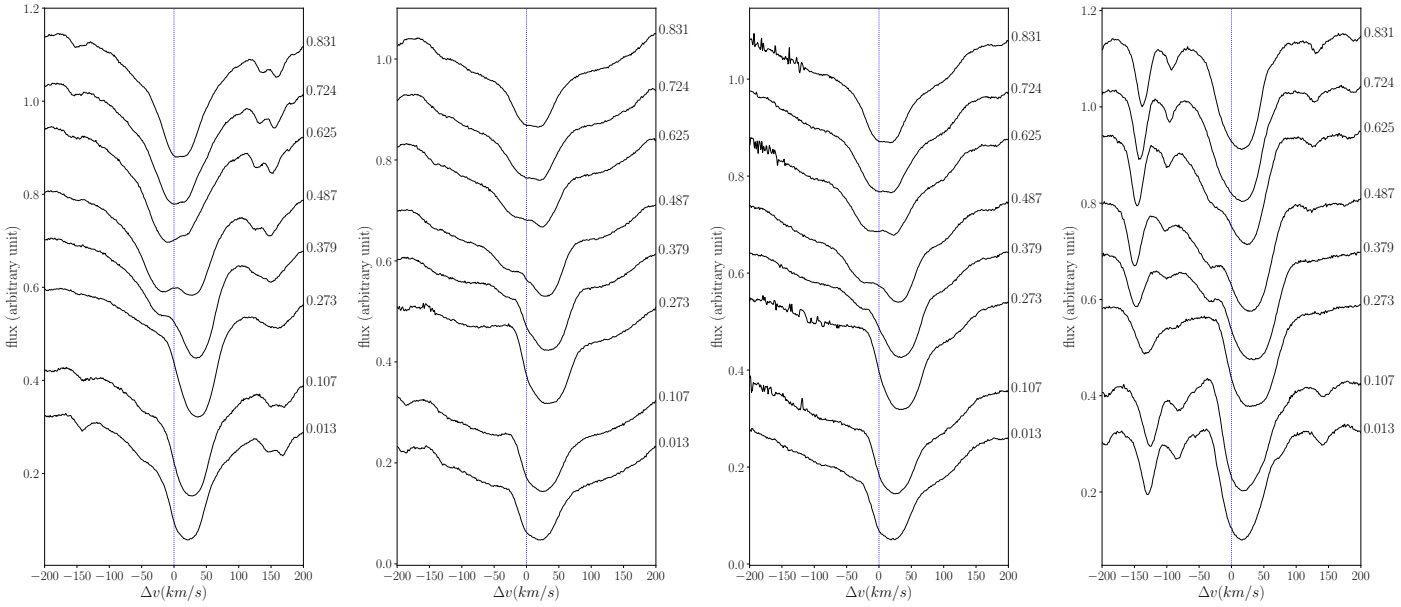

(a) λ8498 (b) λ8542 (c) λ8662 (d) Hα

Fig. B.21. V1496 Aql, 65.37 d.